Remote Sensing of Environment 251 (2020) 112095

Contents lists available at ScienceDirect

Remote Sensing of Environment

journal homepage: www.elsevier.com/locate/rse

A new framework to map fine resolution cropping intensity across the globe: Algorithm, validation, and implication

Chong Liu[a,b,c], Qi Zhang[d], Shiqi Tao[e], Jiaguo Qi[f], Mingjun Ding[g], Qihui Guan[g], Bingfang Wu[b,h,*], Miao Zhang[b,*], Mohsen Nabil[b,h,i], Fuyou Tian[b,h], Hongwei Zeng[b,h], Ning Zhang[j], Ganbat Bavuudorj[b,h,k], Emmanuel Rukundo[b,h], Wenjun Liu[b], José Bofana[b,h,l], Awetahegn Niguse Beyene[b,h,m], Abdelrazek Elnashar[b,h,n]

[a] School of Geospatial Engineering and Science, Sun Yat-Sen University, Guangzhou 510275, PR China
[b] State Key Laboratory of Remote Sensing Science, Aerospace Information Research Institute, Chinese Academy of Sciences, Beijing 100101, PR China
[c] Southern Marine Science and Engineering Guangdong Laboratory (Zhuhai), Zhuhai 519000, PR China
[d] Frederick S. Pardee Center for the Study of Longer-Range Future, Frederick S. Pardee School of Global Studies, Boston University, Boston, MA 02215, USA
[e] Graduate School of Geography, Clark University, Worcester, MA 01610, USA
[f] Center for Global Change and Earth Observations, Michigan State University, East Lansing, MI 48823, USA
[g] School of Geography and Environment, Jiangxi Normal University, Nanchang 332000, PR China
[h] University of Chinese Academy of Sciences, Beijing 100049, PR China
[i] Division of Agriculture Applications, Soils, and Marine (AASMD), National Authority for Remote Sensing & Space Sciences (NARSS), Cairo, New Nozha, Alf Maskan, 1564, Egypt
[j] University of California Agriculture and Natural Resources, Davis, CA 95618, USA
[k] Information and Research Institute of Meteorology, Hydrology and Environment, Ulaanbaatar 15160, Mongolia
[l] Faculty of Agricultural Sciences, Catholic University of Mozambique, Cuamba, Niassa 3305, Mozambique
[m] Tigray Agricultural Research Institute, P.O. Box 492, Mekelle 251, Ethiopia
[n] Department of Natural Resources, Faculty of African Postgraduate Studies, Cairo University, Giza 12613, Egypt

ARTICLE INFO

Keywords:
Cropping intensity
Remote sensing
Multiple sensors
NDVI time series
Crop phenophase

ABSTRACT

Accurate estimation of cropping intensity (CI), an indicator of food production, is well aligned with the ongoing efforts to achieve sustainable development goals (SDGs) under diminishing natural resources. The advancement in satellite remote sensing provides unprecedented opportunities for capturing CI information in a spatially continuous manner. However, challenges remain due to the lack of generalizable algorithms for accurately and efficiently mapping global CI with a fine spatial resolution. In this study, we developed a 30-m planetary-scale CI mapping framework with the reconstructed time series of Normalized Difference Vegetation Index (NDVI) from multiple satellite images. Using a binary crop phenophase profile indicating growing and non-growing periods, we estimated pixel-by-pixel CI by enumerating the total number of valid cropping cycles during the study years. Based on the Google Earth Engine cloud computing platform, we implemented the framework to estimate CI during 2016–2018 in eight geographic regions across continents that are representative of global cropping system diversity. Comparison with PhenoCam network data in four cropland sites suggests that the proposed framework is capable of capturing the seasonal dynamics of cropping practices. Spatially, overall accuracies based on validation samples range from 80.0% to 98.9% across different regions worldwide. Regarding the CI classes, single cropping systems are associated with more robust and less biased estimations than multiple cropping systems. Finally, our CI estimates reveal high agreement with two widely used land surface phenology products, including Vegetation Index and Phenology V004 (VIP4) and Moderate Resolution Imaging Spectroradiometer Land Cover Dynamics (MCD12Q2), meanwhile providing much more spatial details. Due to its robustness, the developed CI framework can be potentially generalized to produce global fine resolution CI products for food security and other applications.

* Corresponding authors at: State Key Laboratory of Remote Sensing Science, Aerospace Information Research Institute, Chinese Academy of Sciences, Beijing 100101, PR China.
E-mail addresses: liuchong5@mail.sysu.edu.cn (C. Liu), wubf@aircas.ac.cn (B. Wu), zhangmiao@aircas.ac.cn (M. Zhang).

https://doi.org/10.1016/j.rse.2020.112095
Received 14 May 2020; Received in revised form 6 September 2020; Accepted 8 September 2020
Available online 18 September 2020

1. Introduction

As one of the 17 sustainable development goals (SDGs) by the United Nations, achieving hunger and poverty eradication is ambitious yet facing many critical challenges. Current world population of 7.7 billion will likely increase by 1 billion in 2030 and possibly approach 10 billion by 2050 (UN, 2015). Such rapid growth in population, along with expanding biofuel uses and changing dietary preferences (Godfray et al., 2010; Kastner et al., 2012), requires a substantial increase in global food production. Given these challenges, the agriculture sector has a greater role than ever to play in meeting the increasing demand and achieving the second SDG: zero hunger. However, increasing agricultural production to satisfy the growing demand is not an easy task. Studies suggest that global agricultural production needs to double its current size within the next three decades to keep pace with the growing needs of human and livestock (Alexandratos and Bruinsma, 2012; Tilman et al., 2011). Although statistics report that the amount of food produced per person has increased by more than 40% since the 1960s with a potentially promising trend, current agriculture strategies have led to many environmental problems, including the occupation of marginal lands and desertification (Qi et al., 2020). At the same time, the high rate of urban expansion over the last three decades has resulted in huge loss of high-quality agricultural land around the world (d'Amour et al., 2017). Without effective strategies to increase agricultural production, the goal of zero hunger remains elusive.

Cropland, whose extent includes growing crops, cropland fallows and plantations (Xiong et al., 2017; Phalke et al., 2020), is an essential asset that undergirds agriculture and hence the focus of food security. There are mainly two strategies for increasing annual crop production with regard to cropland management. The first is to expand cropland area by converting other land covers. For instance, to cope with the huge demand for commercial crops, Brazil's gross cropland area has doubled its size during 2000–2014, mainly through invading pastureland and forest (Zalles et al., 2019). Despite its prominent contribution to increasing food production, cropland expansion is often viewed as an unsustainable strategy because of its environmental consequences including loss of wildlife habitat, land degradation, and greenhouse gas emission (Wu et al., 2018). The second strategy is to intensify the use of the existing cropland. Beginning in the early 1950s with Green Revolution (Pingali, 2012), cropland intensification involves practices that aim to increase outputs of crop(s) per unit area through the use of machinery, fertilizer, pesticide/herbicide, greenhouse, irrigation. Other management practices, such as crop rotation, intercropping, and multiple harvests, are also adopted to leave less land fallow and reduce crop failures (Foley et al., 2011).

Cropping intensity (CI), defined as the number of cropping cycle(s) per year (Li et al., 2014; Gray et al., 2014a), is a key crop growth indicator and thus an important measure of food production. Despite the controversy on environmental impacts of intensive cultivation, the increasing CI plays an essential role in closing the food demand gap and alleviating rural poverty (Iizumi and Ramankutty, 2015; Wu et al., 2018), especially in Asia and Africa where cultivated land resources are severely limited to support large populations (Xie et al., 2019). Information about CI is traditionally generated from existing crop calendar datasets (Siebert et al., 2010) or based on national/regional statistics (Zaks and Kucharik, 2011). Despite their importance in food production assessment, current CI maps are coarse in spatial resolution and variable in accuracy (Liu et al., 2020). The advent of satellite remote sensing has revolutionized our ability to obtain information about agricultural practices. Efforts have been made to extract CI information based on remotely sensed imagery, primarily through the analysis of phenological cycles using high temporal frequency vegetation index time series (Ding et al., 2016). For example, Yan et al. (2014) estimated the CI distribution of mainland China by detecting EVI growing season peaks. This approach was also employed in a more recent study for global CI mapping using Global Inventory Monitoring and Modeling System (GIMMS) NDVI dataset (Chen, 2018). In addition to directly relying on time-series information, other methods including thresholding (Li et al., 2012), supervised classification (Singha et al., 2019) and temporal mixture analysis (Jain et al., 2013) have also been widely adopted for CI identification.

However, to the best of our knowledge, a general framework of global fine resolution CI mapping is still lacking. The median resolution satellite data, such as MODIS is too coarse to capture within-field CI information due to mixed land covers or land uses (Oliphant et al., 2019). Therefore, it becomes increasingly clear that temporally denser, higher spatial resolution data may provide more accurate CI information to capture crop diversity. The open archives of Landsat and Sentinel images offer an unprecedented opportunity for overcoming the obstacles in CI information extraction. These records have greatly promoted the construction of satellite image time series, which can be specialized for and beneficial to CI mapping at larger scales with fine resolutions. Furthermore, the rapid development of cloud computing platforms, such as Google Earth Engine (GEE) (Gorelick et al., 2017), Amazon Web Services (AWS) (Lavreniuk et al., 2018) and Microsoft Azure (Wilder, 2012), eases the workloads of downloading and preprocessing satellite images, thus making global CI mapping feasible. A recent study developed an algorithm that combines Landsat and Sentinel-2 data for mapping annual cropping intensity at the 30-m resolution in mainland China, and the results showed high accuracy in extracting crop cycle at the country level (Liu et al., 2020). Therefore, it is promising to map global CI using a combination of different satellite datasets.

In this study, we take a step forward by developing a new framework of mapping global, fine resolution CI through synergistically integrating Landsat, Sentinel-2 and MODIS data to detect each phenological cycle of annual crops. The primary goal of this study is to demonstrate the efficiency and validity of our framework across different geographic regions around the world. Specifically, we implement the framework on the GEE platform and apply it to eight selected regions from different climate zones that are representative of global cropping system diversity. We compare our results with existing land surface phenology products as well as in-situ data for validation, and discuss the potential of using this framework to operationalize global fine resolution CI products.

2. Study regions and data source

2.1. Study regions

To validate the proposed framework on CI mapping at the global scale, we selected eight $10^{\circ} \times 10^{\circ}$ tiles that consist of a relatively large portion of cropland as study regions (Fig. 1). The selected regions cover all the continents except the Antarctic, and are representative of the diversity of climate zones, cropping systems, and social cultures. To justify the representativeness of these regions for testing and validating our methods, we provide their detailed descriptions as follows.

Africa (AF): The AF tile is situated in Southern Nigeria, Benin, Togo and Ghana where the tropical savanna climate prevails. Most crops are rainfed in this region. The monsoon rainy season normally starts in February/March and ends in October. Cereals (rice and maize), tubers (cassava), and cash crops (oil palm) are commonly cultivated. Most of the farmers are smallholders with little agricultural techniques implemented.

Australia (AS): The AS tile covers the entire Victoria and the south part of New South Wales. Except for its coastal area featured by temperate marine climate, the majority of this region suffers an arid climate with frequent drought (Van Dijk et al., 2013; Wu et al., 2015). Constrained by water availability, the single cropping system is widely distributed. Wheat and barley are major grain crops with large interannual production changes. The sowing period spans from May to June and the harvest period is from October to December.

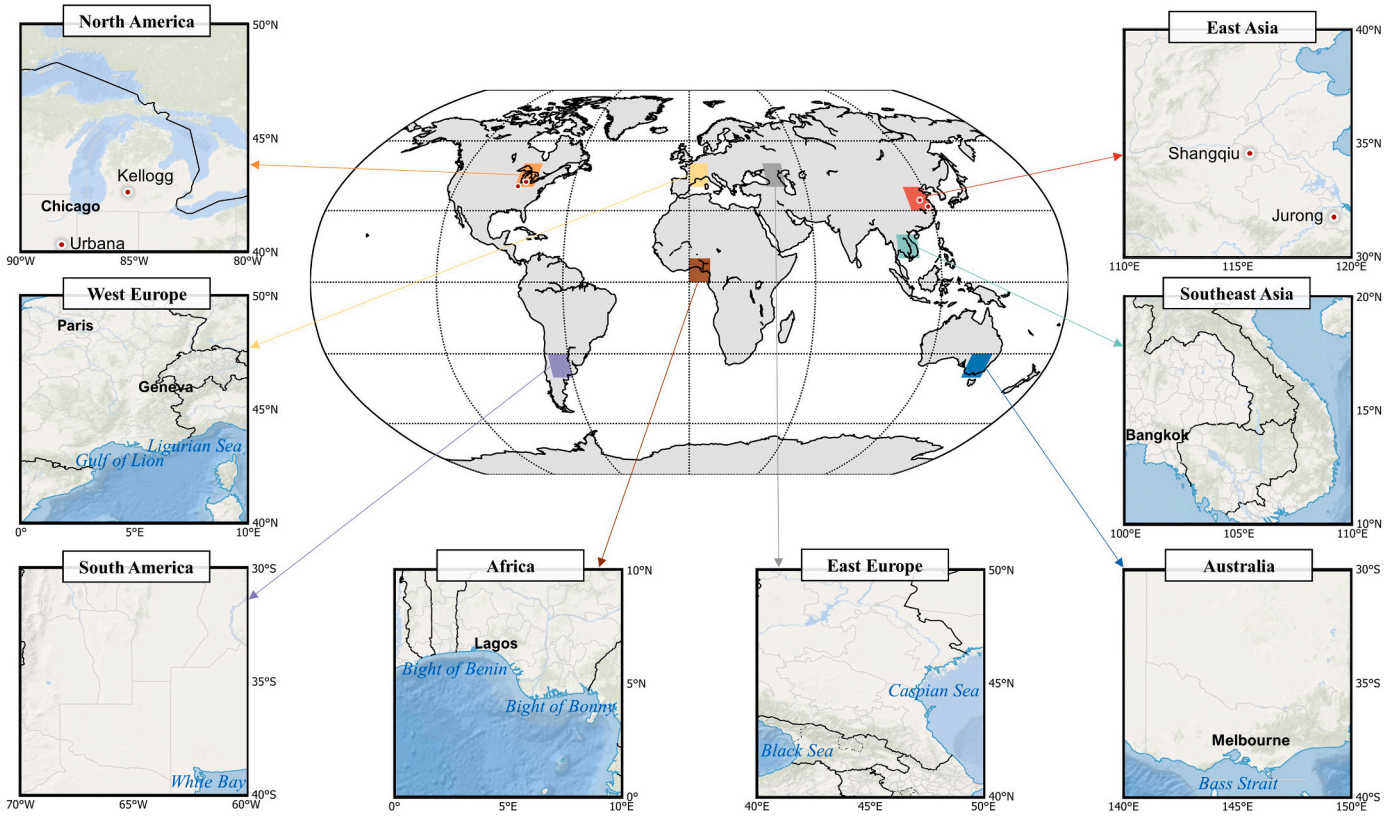

Fig. 1. Eight study regions, with each covering an area of 10° × 10°, are the hotspots of global agriculture featured by diverse cropping systems. The terrain of each region is displayed as the background, with gray representing hill shade, white representing plain, green representing forest, and blue representing water. Red dots in the East Asia and North America tiles represent PhenoCam sites used in this study. (For interpretation of the references to color in this figure legend, the reader is referred to the web version of this article.)

East Asia (EA): The EA tile is located in North China with a warm temperate climate and moderate precipitation ranging from 450-mm to 1000-mm per year. Supported by well-developed irrigation systems, this region is characterized by the wheat-maize double cropping system, leaving a small proportion of croplands occupied by single-season crops, including rice and cotton (Wu et al., 2014).

East Europe (EE): The EE tile covers Southern Russia, Georgia, Azerbaijan and Northeast Turkey. Experiencing a temperate continental climate, both winter crops and summer crops are grown in this region. Winter crops are usually planted during August–October and harvested during July–August in the next year. Summer crops are sown mainly in May and harvested in mid-August or September.

North America (NA): The NA tile is located in the Great Lakes region at the board line between Canada and the United States (U.S.), and featured by a humid continental climate. The fertile land and abundant water supply in this region support a great amount of production of corn, soybeans, hay crops, etc. Corn is actively planted from late April to early June, and harvested from September to December. Soybean, another major crop in NA, is usually planted during early May to middle June, while harvested in October or November.

South America (SA): The SA tile is distributed in Argentina and covers its major agricultural producing provinces. Winter wheat, soybean and maize are the main crops in this region. Winter wheat is usually planted in June, grows across winter and is harvested from November to January next year, while maize is sown during September–December and harvested during March and after. Two types of soybean are cultivated in Argentina: early soybean sown in November and harvested in April, and late soybean sown in January after the harvest of wheat.

Southeast Asia (SEA): The SEA tile encompasses the majority of the lower Mekong River Basin, including Central and Eastern Thailand, Cambodia, Laos, and most parts of Vietnam. Paddy rice is the dominant annual crop type in this region. Due to the large variation in agro-environmental and management conditions, crops grown by farmers are diverse across this region, delivering a more complex situation in terms of cropping systems than the other seven regions. Specifically, farmlands are delimited in relatively small size and managed by different households. Crops are harvested from one to three times within a year.

West Europe (WE): The WE tile includes mainly Spain, France, Switzerland, Italy and Germany, where many places have a temperate climate with plenty of rainfall. Major cereal productions originate from the Paris Basin, where both natural and geographic conditions are favorable for the cropping activities. For winter crops, sowing dates can vary from October to November, while harvesting dates can be between July and August. While summer crops are usually planted in a wide sowing window during April–May, and its harvest period lasts during September–November.

2.2. Satellite data

Satellite data captured and digitalized by Landsat, Sentinel-2, and MODIS were used for CI mapping. Landsat provides the longest, freely accessible earth observation archive, which is the most repeatedly and frequently used source of satellite images capable of covering the entire terrestrial surface (Woodcock et al., 2008). This study used ETM+ images from Landsat-7 and OLI images from Landsat-8, both of which offer continuous spatial data through the study years (2016–2018). Among various Landsat products, we used the category of Collection 1 Tier 1 since it meets the quality standard, rendering itself the most reliable for studies using time series data (Liu et al., 2019). Sentinel-2 MultiSpectral Instrument (MSI) is a relatively new satellite sensor having started observing the earth's terrestrial surface since 2015, while

Table 1
Meta information of four PhenoCam sites used in this study.

Site ID	Latitude	Longtitude	Dominant species	Data start date	Data last date
Jurong	31.8068	119.2173	summer rice-winter wheat rotation	2017-10-21	2019-11-24
Shangqiu	34.5155	115.5950	maize and wheat	2018-01-24	2019-11-24
Kellogg	42.4375	−85.3225	maize	2014-05-24	2019-11-18
Urbana	40.0628	−88.1984	miscanthus	2008-11-11	2019-11-22

it becomes increasingly popular in remote sensing applications due to its relatively high spatial and temporal resolutions. For the purpose of harmonizing images captured by Landsat and Sentinel-2, only top-of-atmosphere (TOA) reflectance data were used; their poor quality or irrelevant observations including cloud, cloud shadow and snow were masked by the Function of mask (Fmask) algorithm (Zhu and Woodcock, 2012; Qiu et al., 2019). To reduce the error caused by missing Landsat and Sentinel-2 observations, we also included the MOD13Q1 V6 NDVI product in the data pool for time series reconstruction. This vegetation index product is composited from the best available pixels from all the acquisitions within 16 days. Despite the relatively low spatial resolution (250-m), MOD13Q1 adds up plenty of signals that are especially useful in high cloud cover areas such as the lower Mekong River Basin in Southeast Asia and Southern Nigeria in Africa. Considering the cross-year growing cycle, the study period was set as three consecutive calendar years from January 2016 to December 2018, while the average number of valid cropping cycles during the three years was calculated as the final output of the annual CI.

2.3. Cropland extent data

In this study, we used Global Food Security-support Analysis Data at 30 m (GFSAD30) to delimit the cropland extent of interest while masking out irrelevant pixels. GFSAD30 provides global cropland/non-cropland identification at the 30-m spatial resolution for the nominal year of 2015 (2010 in North America). This product is divided into separate regional datasets for free access (Oliphant et al., 2019; Gumma et al., 2020; Teluguntla et al., 2018; Xiong et al., 2017). To reduce the bias from individual classification schemes and temporal disagreement between GFSAD30 and the output in our study, we incorporated an ensemble of three additional land cover layers for GFSAD30 refinement. These three land cover products include 25-m PALSAR-2/PALSAR Forest/Non-Forest Map (FNF) for the year of 2017, 30-m JRC Global Surface Water Layer (GSWL) for the year of 2017 and 38-m Global Human Settlement Layers (GHSL) for the year of 2015. FNF and GHSL were re-sized to 30-m from their original spatial resolutions using the majority resampling and bicubic interpolation methods, respectively before refining the cropland class. Based on these layers, we treated the GFSAD30 as the base layer and designed a set of criteria to identify cropland. The criteria are 1) cropland in GFSAD30; 2) non-forest in FNF; 3) non-water in JRC-GSWL, 4) non-built-up in GHSL. Only by satisfying all these criteria can one given pixel be classified as cropland.

2.4. Reference data

Two reference datasets (termed RD-1 and RD-2 hereafter) were constructed to validate the refined cropland extent map and the final CI outputs, respectively (Table S1). For RD-1, we first randomly created 1000 sample points in each study region, then visually identified the classes (cropland or non-cropland) for the period of 2016–2018 based on high resolution Google Earth images. After removing points that were unable to be identified, there remained 765, 750, 874, 710, 513, 925, 787 and 751 sample points for AF, AS, EA, EE, NA, SA, SEA and WE, respectively. For RD-2, the random sampling was applied only to the cropland pixels from the refined cropland extent map. In each study region, 500 points were collected, and their phenological cycles during the period of 2016–2018 were visually counted on the Geo-Wiki platform (http://www.geo-wiki.org/), which enables us to interpret pixel-level NDVI time series from multiple satellite data including Landsat, MODIS and PROBA-V (Bayas et al., 2017). To minimize interpretation bias, we also included other available resources to refine our judgments. For example, in EA, crop calendar and national statistical data of China were collected, while in NA, USDA NASS Cropland Data Layers (CDL) were used as an additional reference. We kept only well-interpreted points with high-level confidence, which eventually led to 48 (AF), 61 (AS), 90 (EA), 76 (EE), 68 (NA), 75 (SA), 85 (SEA), and 54 (WE) sample points, respectively.

In addition to the generated reference samples, we further obtained three auxiliary datasets. The first is the PhenoCam network (Richardson et al., 2018), which is widely used as a robust ground reference for remotely sensed phenology metric validation. Currently, there are only four PhenoCam sites on cropland within our selected regions (Table 1), hence all of them were incorporated in this study. Within the PhenoCam dataset v2.0 (Seyednasrollah et al., 2019), we used mainly the green chromatic coordinate (GCC) index (Richardson et al., 2018) and in-situ phenology camera image time series for cropping cycle identification. For a region of interest, the GCC index value is calculated as:

$$GCC = \frac{G_{DN}}{R_{DN} + G_{DN} + B_{DN}} \quad (1)$$

Where R_{DN}, G_{DN} and B_{DN} denote the average red, green and blue digital numbers from camera image channels. The original, sub-daily GCC time series are further composited by calculating the 90th percentile at 1-day and 3-day intervals, respectively. We used only the 3-day GCC product because it minimizes high-frequency noise (Zhang et al., 2018; Seyednasrollah et al., 2019; Qiu et al., 2020).

The second auxiliary product is NASA's Vegetation Index and Phenology V004 (VIP4) dataset (Didan and Barreto, 2016). This dataset provides yearly global vegetation indices and phenology metrics from 1981 to 2014 at a spatial resolution of 0.05°. To minimize uncertainty caused by temporal disagreement, we selected only the 2014 VIP4 data, within which the layer of the Number of Seasons (ranging from 0 to 3) was pulled out to support our validation. The third product is MODIS Land Cover Dynamics (MCD12Q2) Version 6, which provides global land surface phenology metrics at the 500-m resolution and annual interval from 2001 to 2017 (Gray et al., 2019). We chose the 2016 and 2017 MCD12Q2, within which the layer of NumCycles was extracted, and their annual average result was compared to our CI estimation.

3. Methods

Fig. 2 shows the developed framework that aims to utilize pixel-level time-series information for global CI mapping on the GEE platform. The framework can be divided into three sequentially integrated parts. In the first part, we fuse data from multiple satellite instruments, including Landsat, Sentinel-2 and MODIS, to generate a smoothed NDVI image time series dataset at the 30-m resolution with a 16-day interval. The second part characterizes the seasonal change of cropping practices by dividing the entire NDVI time series profile into a temporal sequence of staggered segments of growing or non-growing periods. Finally, we derive the CI value of each pixel by enumerating the transition points between different periods. Detailed procedures within the framework are described below.

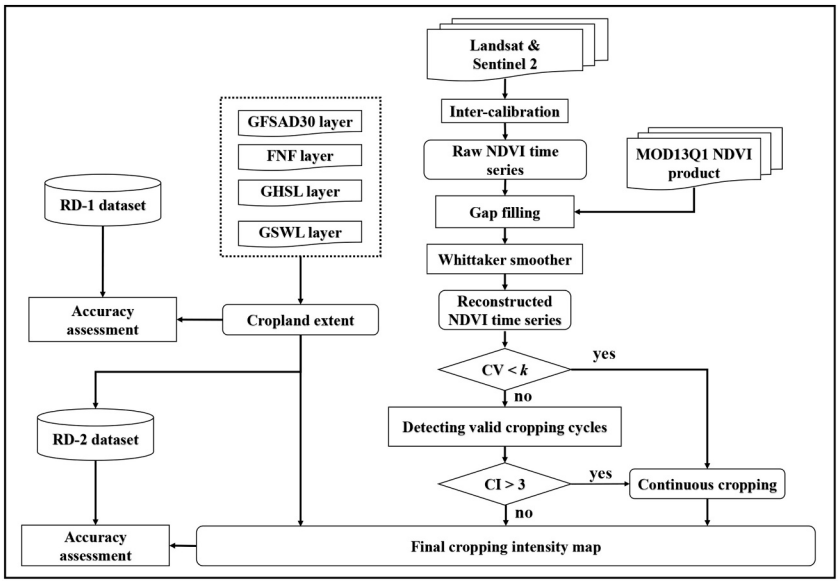

Fig. 2. Flow chart of cropping intensity mapping through multi-source data fusion and phenological cycle depiction. CV and CI denote coefficient of variation and cropping intensity, respectively. The symbol of k is the threshold derived as the average CV value of continuous cropping samples from RD-2.

3.1. Harmonization of multi-source NDVI time series

3.1.1. Integration of Sentinel-2 and Landsat TOA reflectance data

Fine spatial resolution images from different satellite sensors, such as Landsat and Sentinel-2, bear with inconsistency in terms of the measured spectral features (Claverie et al., 2018). To overcome this multi-sensor mismatch, an inter-calibration approach was performed. According to Chastain et al. (2019), we converted Sentinel-2 MSI and Landsat-8 OLI TOA reflectance to the standard of Landsat-7 ETM+ using empirical transformation functions. These functions were built from statistical relationships between the obtained signals of equivalent multi-sensor spectral bands, possessing the advantage of simplifying processing workflows (Chastain et al., 2019; Scheffler et al., 2020). Based on the calibrated TOA reflectance observations, we calculated their NDVI values. Eventually, a 16-day NDVI composite was obtained by deriving the median value of all valid observations (i.e., free of clouds, cloud shadows, and snow) during each interval.

3.1.2. Gap filling with MOD13Q1

Even for fused and composited time series, missing values remain due to the vacancy of valid fine resolution satellite observations with a time length longer than 16 days. These gaps could undermine or even lead to the failure of CI detection. To ensure data continuity, this study used the MOD13Q1 NDVI product to fill temporal gaps with the following steps. First, the 250-m MOD13Q1 NDVI product was re-sized to 30-m using the bicubic interpolation algorithm. Then, based on pairs of the resampled MOD13Q1 and the fine resolution satellite observations that were both valid and acquired within the same interval (i.e., 16-day), the linear function of NDVI adjustment was derived for each pixel:

$$\boldsymbol{Y} = a\boldsymbol{X} + b \tag{2}$$

where $\boldsymbol{X}$ and $\boldsymbol{Y}$ denote NDVI time series of original and transformed MOD13Q1 NDVI, respectively; a and b are estimated coefficients (slope and intercept) using the least square method. Finally, missing data gaps were filled using the resampled, adjusted MOD13Q1 NDVI data. Since we used only the MOD13Q1 data in high quality, i.e., the SummaryQA band values are 0 (good) or 1 (marginal), an extreme case may exist, that is, in a 16-day interval there is no valid data from either fine resolution satellites or MODIS. In this case, the filling NDVI value was determined by temporally adjacent (within 48-day) clear-sky fine resolution observations using linear interpolation. Therefore, the gap-filling process results in a composited NDVI time series consisting of: 1) Landsat/Sentinel-2 harmonized observations (origin), 2) MODIS modeled values (MODIS modeled), and 3) interpolated values using adjacent observations (interpolated).

3.1.3. NDVI time series reconstruction with weighted Whittaker smoother

The gap filled NDVI time series is comprised of segments connected by sequentially individual points, hence required smoothing. In this study, the Whittaker algorithm (Whittaker, 1922) was utilized to smooth the NDVI time series. Compared to other smoothers, such as double logistic and Asymmetric Gaussian, the Whittaker smoother has the advantage in balancing fidelity and roughness (Eilers, 2003). More importantly, it is computationally efficient, allowing users to implement it on the GEE platform for global-scale applications (Kong et al., 2019). A key parameter of the Whittaker smoother is λ, which quantifies the degree of smoothness. A large value of λ indicates a stronger effort of smoothing, which nevertheless compromises the changing magnitude; a smaller λ value has less degree of smoothing, yet with less risk of eliminating the actually abrupt change(s). We employed the "V-curve" method (Frasso and Eilers, 2015; Eilers et al., 2017) and NDVI time-series data from RD-2 to seek the optimal λ. To deal with NDVI outliers, we included a weight updating procedure in the smoothing algorithm. Specifically, we assigned initial weights of 1, 0.5, and 0.2 with respect to Landsat/Sentinel-2 observations, MODIS modeled values and interpolation values. The assigned weights reflect the reliability of the above-mentioned data, following the order of origin > MODIS modeled > interpolated. Then the bisquare function (Gross, 1977) was used for weights updating according to the residual between smoothed and actual observations. This operation was repeated until the maximum number of iterations (set at 2 in this study) was reached. More details on the weighted Whittaker smoother can be found in Kong et al. (2019).

3.2. Creation of cropping intensity map

3.2.1. Determination of phenophase

Traditionally, CI was acquired from satellite sensors by detecting greenness peaks in a given time frame (Gray et al., 2014a; Li et al., 2014; Liu et al., 2020). This approach is straightforward but sensitive to time series noise. Therefore, additional rules are usually needed to eliminate spuriously identified vegetation cycles (Yan et al., 2014,

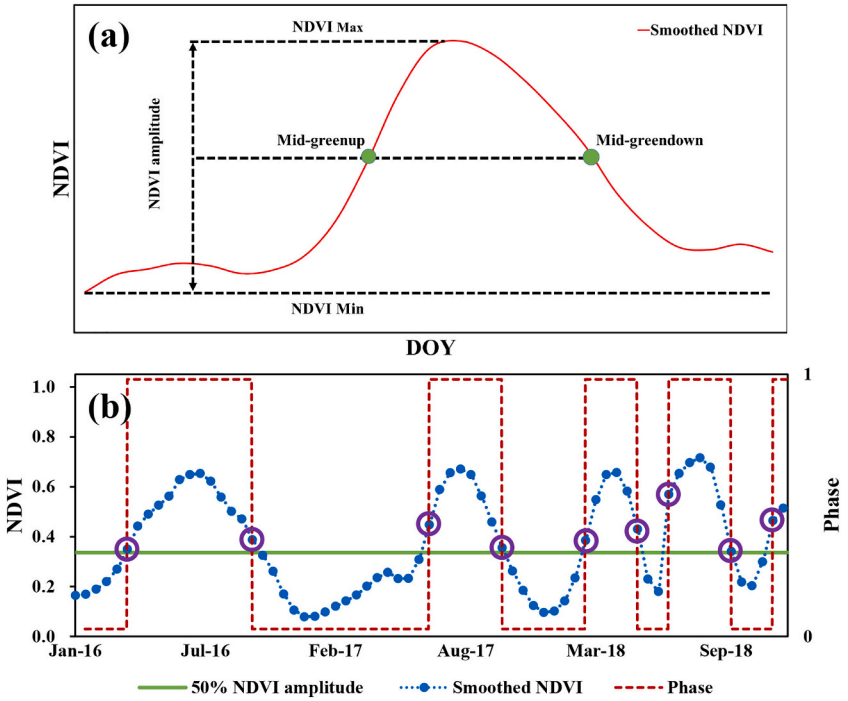

Fig. 3. Illustration of (a) identification of transition points (mid-greenup and mid-greendown) using 50% of the NDVI amplitude as the threshold and (b) generating binary phenophase time series.

2019). These subjective processes substantially hamper the CI mapping application at the global scale. To address this issue, here we developed a new CI identification method, aiming to make it more self-adaptive through directly counting the number of growing seasons. Fig. 3 graphically depicts the determination of phenophase(s) at one cropland pixel. First, we derived the minimum and maximum values of the entire study years to characterize the amplitude smoothed NDVI time series. Then, we included two phenology metrics, mid-greenup and mid-greendown, which were derived as the day of year (DOY) at the transition points in the greenup and greendown periods when the smoothed NDVI time series passes 50% of the NDVI amplitude (Bolton et al., 2020). Note that the defined transition points at DOYs are unlikely located at the exact thresholding line (i.e., 50% green line in Fig. 3); so we selected the nearest point (purple circles in Fig. 3) corresponding to a DOY record above the threshold as the transition point, reflecting the transitions within the greenup period of a complete cycle. Finally, these transition points were used to create a new binary time series profile, indicating the crop phenophase (growing as 1, non-growing as 0) at each temporal interval. An interval starting from mid-greenup and ending at mid-greendown is defined as a growing phenophase, and an interval moving from mid-greendown to mid-greenup a non-growing phenophase.

3.2.2. Detection of cropping cycle(s)

Based on the generated phenophase profile and corresponding transition points across 2016–2018, we derived the CI information as follows. First, the number of potential cropping cycles was calculated as:

$$N_{pc} = min\{N_{up}, N_{down}\} \tag{3}$$

where N_{pc} is the number of the potential cropping cycles; N_{up} and N_{down} are the numbers of mid-greenup and mid-greendown transition points, respectively. It should be noted that this potential number may include cycles falsely detected due to the impact of NDVI time series outliers even though the smoothing procedure had been applied. A distinct characteristic of these false cycles is the unrealistic shortness of the periods (Yan et al., 2014, 2019), so we removed the false cropping cycle (s) by setting a lower limit of growing period to 48 days (Sakti and Takeuchi, 2018). Hence, the actual annual CI is:

$$\mathrm{CI} = {(N_{pc} - N_{fc})}/{3} \tag{4}$$

where N_{pc} is the number of potential cropping cycle(s), N_{fc} is the number of detected false cropping cycle(s), and the number 3 is the length of the study period of 2016–2018.

Continuous cropping is very special because it usually shows a shorter growing period (e.g., vegetables) or a less degree of seasonality (e.g., evergreen cash crops) compared with other cropping systems (Fig. S1). Therefore, we included an additional approach for better mapping of continuous cropping lands. For a given pixel *i*:

$$g(i) = \begin{cases} 1 \ \mathrm{CI} > 3 \ or \ \mathrm{CV} < k \\ 0 \ otherwise \end{cases} \tag{5}$$

where $g(i)$ denotes the discriminant function of continuous cropping of pixel *i*; CV is the coefficient of variation (the ratio of the standard deviation to the mean) of the smoothed NDVI time series; k is the threshold calculated as the average CV value of continuous cropping samples from RD-2. Considering the geographical environment difference, the k threshold was calculated separately for each study region.

3.2.3. Framework implementation on the GEE platform

We implemented our methods under the proposed framework using GEE, a cloud-based computing platform that enables massive computational capabilities for geospatial data (Gorelick et al., 2017). We accessed all available Landsat-7, Landsat-8, Sentinel-2 and MODIS image collections with identification indices of "LANDSAT/LE07/C01/T1_TOA", "LANDSAT/LC08/C01/T1_TOA", "COPERNICUS/S2", and "MODIS/006/MOD13Q1", respectively. Then the image collections were clipped to the extents of the study regions and filtered by the study years. Since the current version of the GFSAD30 product is not available on GEE, we downloaded the eight 10° × 10° GFSAD30 tiles covering our study regions from the USGS (https://lpdaac.usgs.gov/tools/data-pool/), and uploaded these tiles to GEE Assets before conducting cropland extent refinement. Other datasets for cropland extent

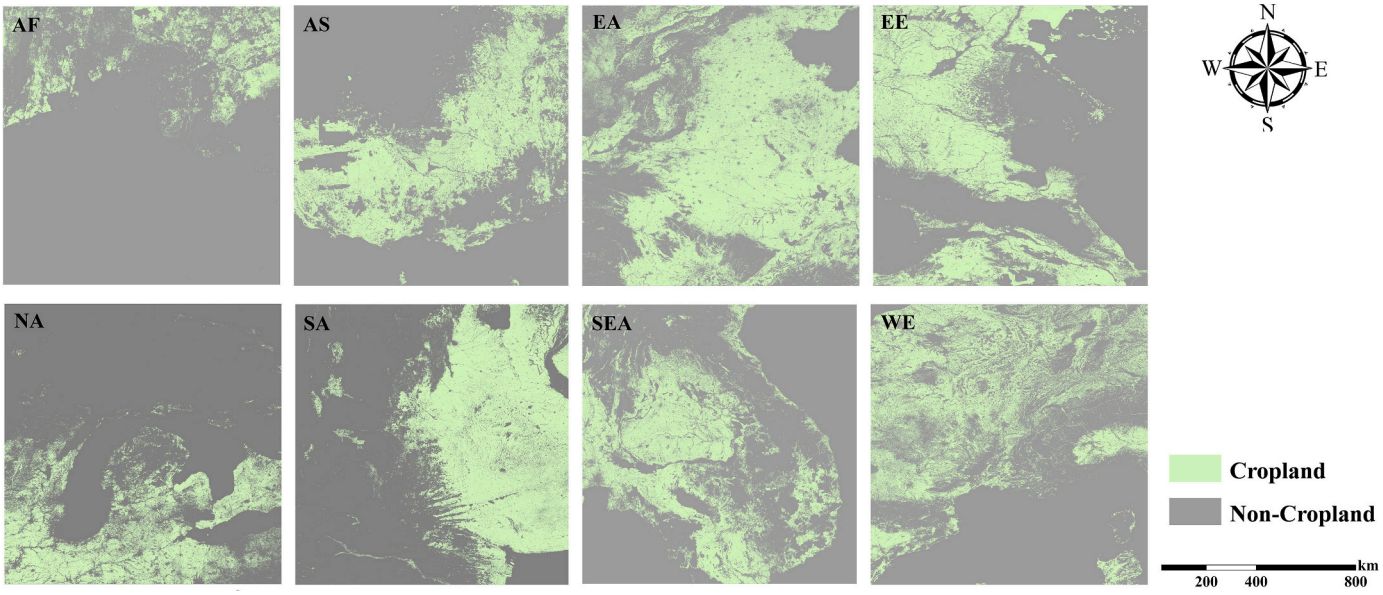

Fig. 4. Spatial pattern of the cropland extent in each study region.

refinement, including FNF, JRC-GSWL and GHSL, were accessed from GEE's public data archive. Codes for mapping CI under the proposed framework were executed separately in each study region. The final results were exported at the 30-m resolution.

3.3. Assessment of CI detection

3.3.1. Refined cropland extent

Based on the reference samples of RD-1, accuracy assessment of the refined cropland extent in each study region was conducted by calculating the confusion matrix and quantitative metrics, including overall accuracy (OA), producer's accuracy (PA) and user's accuracy (UA). To further test the balance of commission and omission errors, we also calculated the minimum accuracy (MA), which is defined as the minimum of PA and UA for all classes (Zhu et al., 2016; Liu et al., 2018; Xu et al., 2018).

3.3.2. Smoothed NDVI time series

Since there are no field measurements of radiance or reflectance at the sites of the collected samples (RD-2), directly validating the quality of the smoothed NDVI time series is impracticable. Alternatively, we evaluated the smoothed NDVI time series by comparing it with the actual clear-sky NDVI observations (Zhang, 2015) derived from the calibrated Landsat and Sentinel-2 TOA reflectance data. Based on the reference samples of RD-2, the agreement between the smoothed and actual NDVI time series was quantified by the Taylor diagram (Taylor, 2001; Zhang et al., 2016). The Taylor diagram exhibits three statistics: the Pearson's correlation coefficient (r), the root-mean-square error normalized by reference standard deviation (nRMSE), and the ratio of smoothed to actual standard deviation (nSTD). According to the proportion of clear-sky observations, we divided the samples into eight groups (namely clear-sky observation percentage of 60%–65%, 65%–70%, 75%–80%, 80%–85%, 85%–90%, 90%–95%, 95%–100%, respectively), and analyzed their performances in the Taylor diagrams.

3.3.3. Cropping intensity maps

Accuracy assessment for the created CI maps was performed in three ways. First, we applied the proposed framework in the four selected PhenoCam sites, and evaluated our results using the 3-day composite 90th GCC indices and in-situ phenology camera image time series. Due to the limited number of PhenoCam sites, we conducted a second validation method using the RD-2 samples. We generated the scatter plot of predicted and reference CI in each region, and evaluated the performance using two indicators: the coefficient of determination (R^2) and root-mean-square error (RMSE). In addition to directly measuring the CI errors, we re-grouped the CI results into four classes: single cropping ($0 < CI \leq 1$), double cropping ($1 < CI \leq 2$), triple cropping ($2 < CI \leq 3$) and continuous cropping, and derived the corresponding confusion matrix as well as quantitative metrics including OA, PA, UA and MA. In the third validation method, NASA's VIP4 and MCD12Q2 datasets were used to evaluate the performance of the CI maps, respectively. First, the CI maps were downscaled to 0.05° and 500-m, respectively, using the majority algorithm to fit the spatial resolution of VIP4 and MCD12Q2. We then recreated CI maps using the ceiling function that rounds the input value to the nearest integer greater than or equal to the input. This reclassification procedure transformed the actual CI to match the VIP4 dataset's value range (0,1,2,3), except for the continuous cropping pixels, which were excluded in this comparison. As a final step, maps of the difference between the reclassified CI and the two reference products, separately, were derived in each study region for visual interpretation and statistical analysis.

4. Results

4.1. Assessment of cropland extent

Fig. 4 shows the binary cropland/non-cropland maps of the eight study regions. In general, all maps are in accordance with visual interpretation, with the percentage of cropland ranging from 8.98% to 51.81% across different continents. Within the study regions, major cropping zones are commonly found in plain areas featured by sufficient water supply (e.g., the North China Plain in EA, the U.S. Great Lakes region in NA, and the Khorat Plateau in SEA). Among all study regions, AF bears special attention. Small-piece cropland clusters are scattered in Togo, Benin and Southern Nigeria characterized by heterogeneous landscapes, indicating a dominant role played by smallholder farms in this region.

Fig. 5 displays the results of accuracy assessment for the refined cropland extent used in this study. In general, we found the classifications of cropland and non-cropland of all study regions have high accuracies, with OA ranging from 88.0% (EE) to 92.8% (NA). Similarly, most study regions exhibit satisfactory MA results (above 80%), except for AF (76.1%) and SA (79.7%) with less desirable results. Compared to the non-cropland class, including forest, urban, and water, the cropland

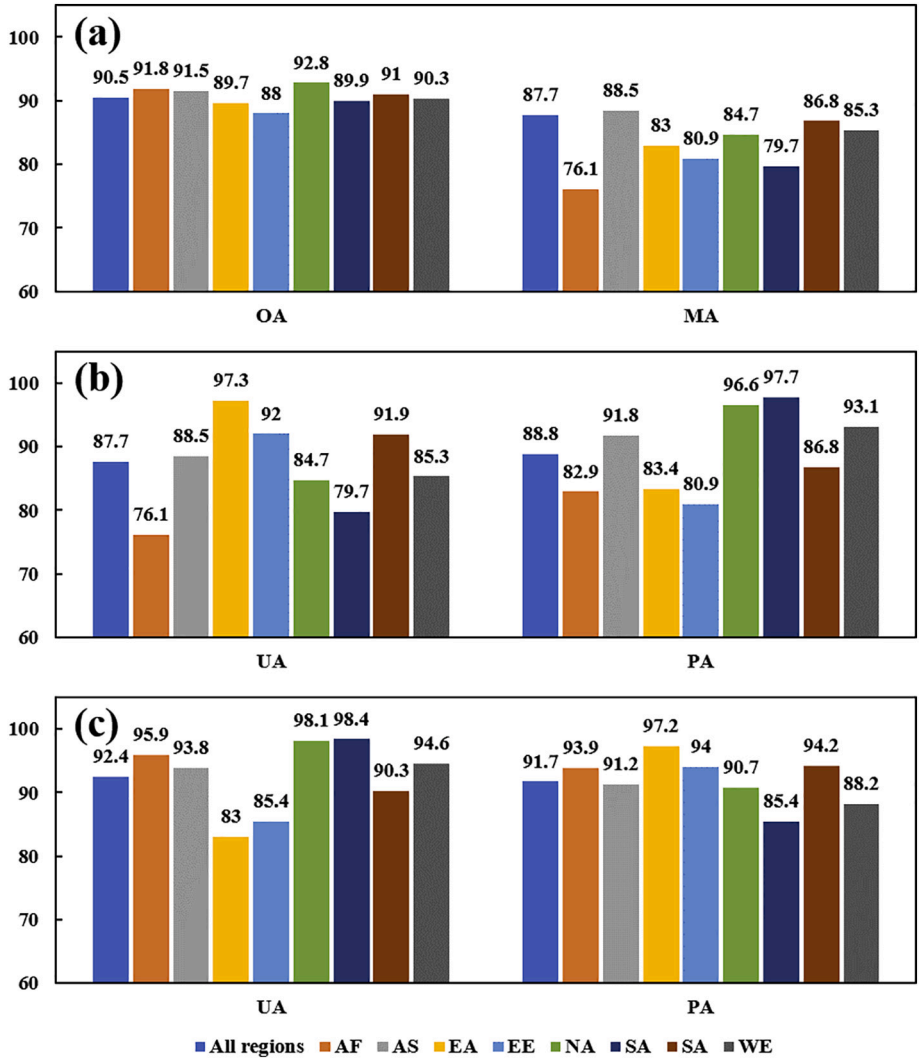

Fig. 5. Accuracy assessments of the cropland extent. (a) overall performance; (b) cropland performance; (c) non-cropland performance.

class displays a greater variation between PA and UA. More specifically, there are five regions (AF, AS, NA, SA and WE) showing higher PA accuracies than UA accuracies, suggesting a tendency of high commission errors in these regions. On the contrary, in EA, EE and SEA, accuracies measured by PA are slightly lower than those by UA, suggesting a tendency of high omission error in these regions.

4.2. Evaluation of smoothed NDVI time series

Fig. 6 shows the Taylor diagrams of performance evaluation for the multi-source NDVI time series harmonization, which is estimated by the actual clear-sky NDVI observations based on the RD-2 dataset. In each diagram, the black point is the reference, and the distance between black and colored dots is the normalized root-mean-square error (nRMSE) between the observed and harmonized values at each RD-2 sample. The dashed line shown in purple is the nRMSE contour, with a 0.1 increment. The radial direction indicates the ratio of harmonized to observed standard deviation (nSTD). The cosine of the angle from the X axis is the coefficient of correlation (r) between harmonized value and observed value depicted in dark green. Therefore, an ideal result would be infinitely approaching the black dot with both nSTD and r close to 1 and nRMSE close to 0. Based on these settings, we interpret the multi-source NDVI time series harmonization performance in each study region. Overall, the harmonized NDVI time-series data match well with the actual observations for most RD-2 samples, although admittedly, there are few outliners featured by low r levels and high nRMSE values. Meanwhile, the majority of harmonized NDVI time series results spread over a wider range with their nSTD greater than 1. We also found that the performances in low latitude regions (AF and SEA) are relatively poor compared with the other regions in middle or high latitudes. For example, we found 78.2% of the samples in EA showed r values higher than 0.9 and nRMSE less than 0.6, while only 60.8% samples in SEA reach the same criteria. Such differences in performance may be explained by the unfavorable atmospheric conditions in low latitude regions. This also explains why samples with higher clear observation percentages (e.g., 95%–100%) exhibit smaller biases.

4.3. Performance of cropping intensity maps

4.3.1. Validation in PhenoCam sites

We evaluated the performance of the extracted CI outputs by referring to ground-based observations obtained from the four PhenoCam sites, and the results are displayed in Fig. 7. For better identification of cropping cycles, both GCC and the corresponding digital camera imagery time series are provided. We found that the estimated CIs are reliable in reflecting cropping cycles across the four different sites. In the Jurong site, both PhenoCam datasets and our estimation detect a single cropping season from 2017 to 2018. Interestingly, the emergence of weeds from March to May in 2018, captured by the camera imagery, had little impact on the smoothed NDVI profile, indicating that our

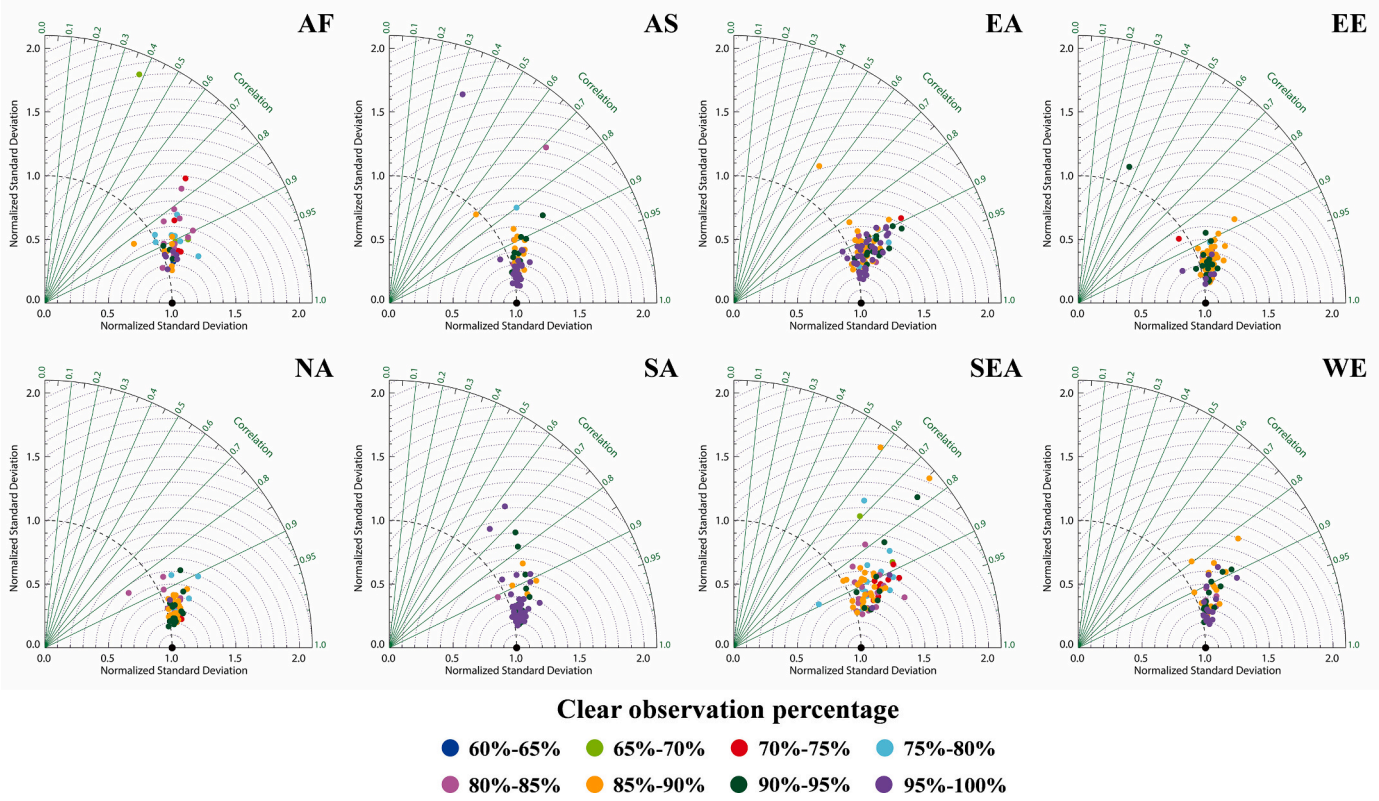

Fig. 6. Taylor diagrams for the performance of multi-source NDVI time-series harmonization. The estimation is based on the actual clear-sky NDVI observations from the RD-2 dataset. The black dot is the reference dot, which has the highest *r* (i.e., the value of 1), the mean level of the nSTD (i.e., value of 1), and the minimum nRMSE of 0. The purple dashed lines denote different levels of nRSME with a circle radius interval of 0.1. This figure was generated using IDLdoc 3.5.0 (http://idlcoyote.com/idldoc/cg/cgtaylordiagram.html). (For interpretation of the references to color in this figure legend, the reader is referred to the web version of this article.)

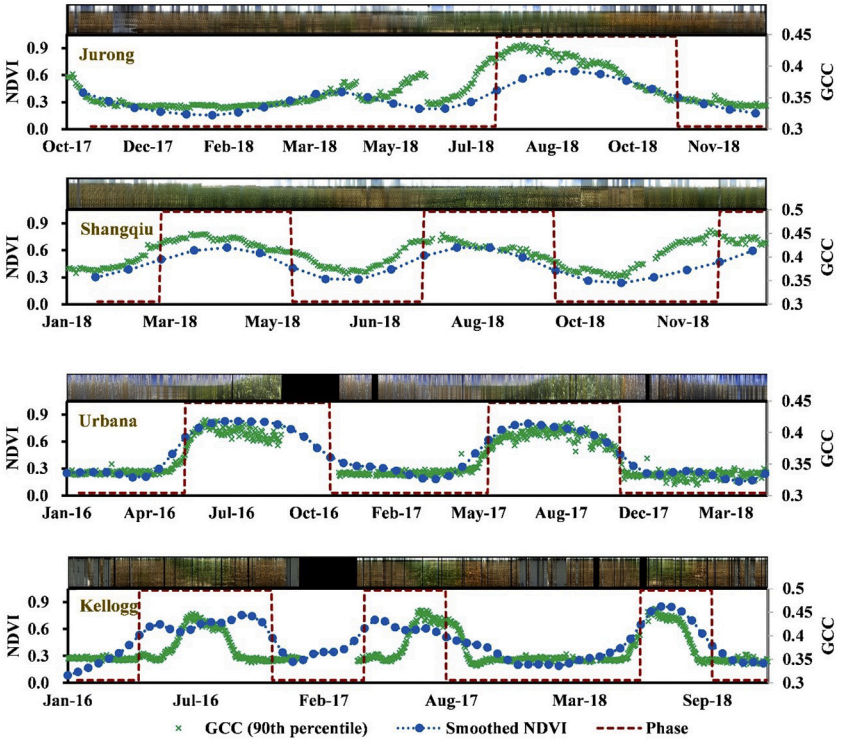

Fig. 7. Evaluation of the extracted CI results in the four PhenoCam sites. The black gaps in digital camera imagery records are caused by missing data.

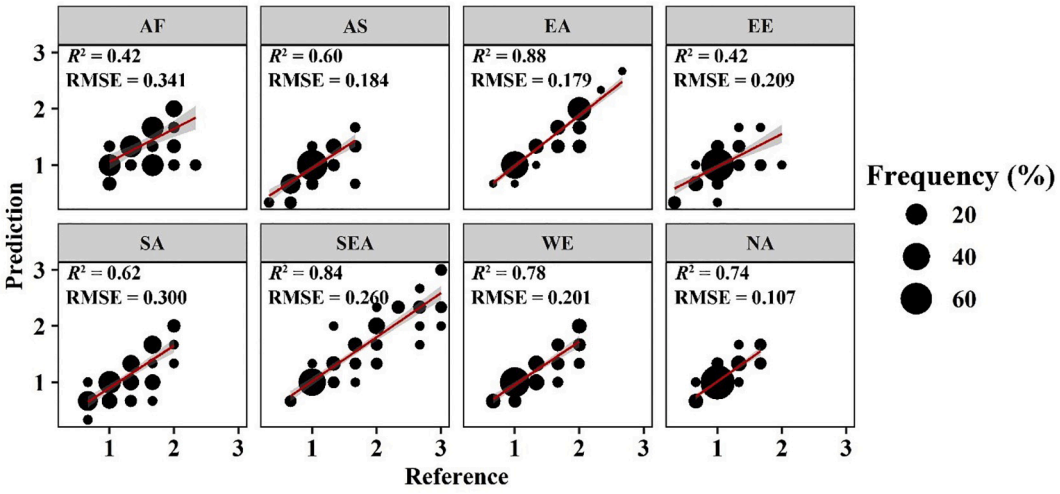

Fig. 8. Scatter plots of CI values based on our estimation and reference data. The red line and the shaded area represent the linear fitting line and 95% confidence interval, respectively. The frequency of specific CI value is proportional to its point size. Samples identified as continuous cropping type are excluded. (For interpretation of the references to color in this figure legend, the reader is referred to the web version of this article.)

algorithm is relatively robust against background noises. In the Shangqiu site, the temporal patterns in NDVI and GCC are close: crop growth reaches peaks in April, August and December, and approaches troughs in June and October. Similarly, in the Urbana site, the NDVI and GCC time series match well with each other, both identifying two distinct cropping cycles from January 2016 to March 2018. The Kellogg site exhibits the largest temporal discrepancy between the NDVI and GCC profiles. This disagreement may be attributed to the scale mismatch between PhenoCam datasets and satellite observations (Moon et al., 2019; Bolton et al., 2020). To further confirm this mismatch, we compared land cover conditions of the four PhenoCam sites (Fig. S2), and noted that the Kellogg site is featured by a more heterogeneous landscape, where sub-pixel spectral signatures of non-cropland covers may contaminate those of cropland within the 30-m NDVI pixel.

4.3.2. Validation with collected samples

We also examined CI accuracy by generating a scatter plot of predicted and reference CI derived from RD-2 samples in each study region. RMSE and R^2 are used as two complementary indicators for quantifying the performance. Overall, our CI results well capture the variations of the reference data (Fig. 8), suggesting that the created CI maps can provide reliable estimations across different continents. Referring to R^2, the best performance is observed in EA (0.88), followed by SEA (0.84), WE (0.78) and NA (0.74), whereas AF (0.42) and EE (0.42) display comparatively weak correlations. Referring to RMSE, better performances are commonly found in regions dominated by the single cropping type (e.g., EE, NA, AS and WE). In contrast, larger estimation errors are mainly distributed in regions where diverse CI types coexist, particularly in AF and SA with RMSEs of 0.341 and 0.300, respectively.

Based on the reclassification procedure illustrated in Section 3.3.3, we derived the corresponding confusion matrix of the generated CI maps based on the RD-2 samples, and the quantitative accuracy metrics are shown in Table 2. We found all study regions have reasonable classification performances, with OAs being equal to or greater than 80.0% and MAs ranging from 50.0% to 83.3%. In general, as expected, regions with less CI types exhibit better accuracy metrics than regions featured by more complex CI compositions. Regarding the classes of CI, we found that the single cropping class is more subject to commission errors than omission errors (PA > UA), meaning a higher probability of overestimation for the single cropping class; in contrast, the opposite tendency (PA < UA) is observed for the multiple cropping classes (double, triple and continuous), which indicates an underestimation of the multiple cropping system. This accuracy assessment by class reflects an overall conservative estimation by our methods, as more actual multiple cropping classes tend to be classified as the single cropping class rather than the other way. In the meantime, the triple and continuous cropping classes exhibit wider variations between PA and UA accuracies (especially the continuous class ranging from 50.0% to 100%), which is mainly due to the limited sample sizes for these classes. For example, in AF, the total number of continuous cropping samples for validation is only four (Table S1), of which two are actually non-continuous cropping class but incorrectly classified as continuous class leading to a commission error of 50%. This limitation originates from the rarity of such cases (i.e., continuous cropping systems) in reality, and we expect a higher, more consistent accuracy level as more samples become available.

Table 2
Accuracy assessment of CI results based on confusion matrix.

Region	Class	UA%	PA%	OA%	MA%
AF	Single	68.8	84.6	80.0	50.0
	Double	85.2	85.2		
	Continuous	100.0	50.0		
AS	Single	94.1	97.9	93.3	70.0
	Double	87.5	70.0		
	Continuous	100	100		
EA	Single	97.5	100.0	98.9	97.5
	Double	100.0	97.9		
	Triple	100	100		
EE	Single	92.6	95.5	89.5	50.0
	Double	62.5	50.0		
NA	Single	96.5	98.2	95.6	83.3
	Double	90.9	83.3		
SA	Single	70.8	100	80.6	60.0
	Double	100	60.0		
	Continuous	100	100		
SEA	Single	91.4	96.9	89.9	78.6
	Double	84.6	84.6		
	Triple	91.7	78.6		
	Continuous	100	100		
WE	Single	86.1	100	90.4	73.7
	Double	100.0	73.7		
	Continuous	100	100		
Total	Single	89.2	97.5	90.4	76.5
	Double	92.0	79.8		
	Triple	92.9	76.5		
	Continuous	100	87.5		

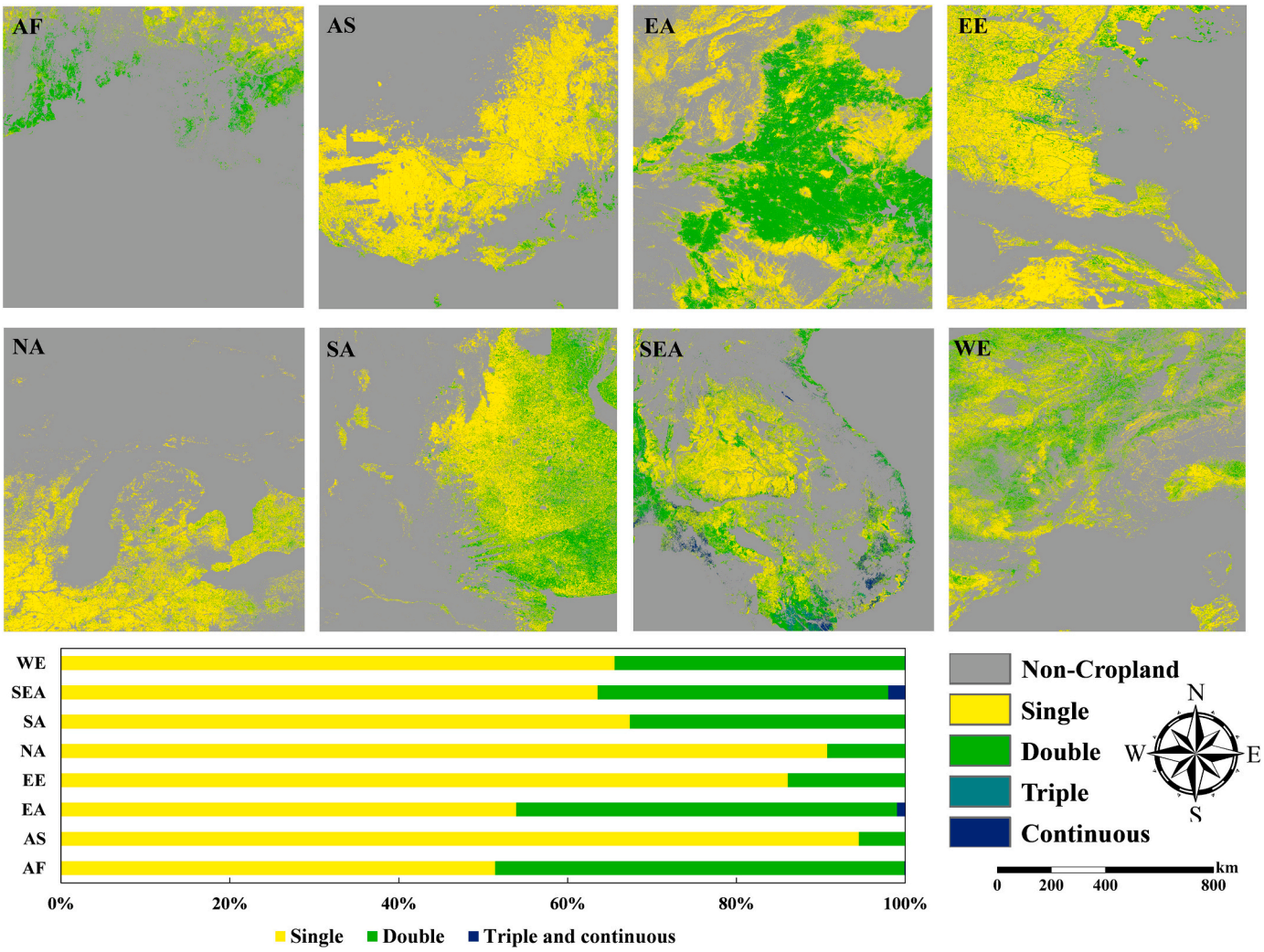

Fig. 9. Spatial pattern and composition of the CI map in each study region. To facilitate analysis, original CI values are re-grouped into four classes: single ($0 < CI \leq 1$), double ($1 < CI \leq 2$), triple ($2 < CI \leq 3$) and continuous.

4.3.3. Spatial patterns and composition of cropping intensity

Fig. 9 shows the spatial pattern and composition of CI for each study region at the 30-m resolution. Overall, single cropping is the primary agriculture system, accounting for more than half of the cropland area in all regions. Double cropping, on the other hand, is typically applied in tropical zones (AF and SEA) and intensive farming regions (EA and WE). Comparably, triple and continuous cropping plays a minor role with limited area occupation, especially in Asia (EA and SEA).

There also exist differences in CI spatial patterns and compositions across the eight regions, which are subject to varying biophysical and anthropogenic conditions such as climate, topography, crop species and agricultural systems. In AF where single and double cropping are almost half and half, single cropping lands are commonly found in relatively arid central Nigeria, while double cropping lands are clustered in the humid southern flat areas. Similarly, single and double cropping systems are the dominant practices in the EA, SA and WE regions. In particular, for EA, SA and WE, the proportions of single cropping in the total cropland area are 53.9%, 67.4% and 65.6%, while the proportions of double cropping are 45.1%, 32.6% and 34.4%, respectively, which appear to be related to topographic characteristics. For example, in EA, double cropping dominated the central part where the topography is fairly flat, leaving the single cropping mostly in the fringe. Among all the study regions, SEA has the most complex CI pattern, encompassing all identified cropping types. Spatially, single cropping (63.5% of the total area) is mainly found in the Khorat Plateau, while double cropping (34.4%) pixels are clustered in the Mekong River Delta, the Red River Delta and Central Thailand. Moreover, SEA is the only region with over 2% of cropland pixels identified as triple and continuous cropping types. AS, NA and EE, all of which are located in the middle latitude zones with temperate climates, display relatively homogeneous CI patterns with the prevalence of single cropping (> 80%).

4.3.4. Agreement with VIP4 and MCD12Q2

Before the comparison between our estimated CI outcomes with existing products, it should be emphasized that neither VIP4 nor MCD12Q2 are considered as ground truth due primarily to their temporal mismatches and coarse spatial resolutions. Instead, the comparisons offer an overall insight of agreement by treating these two products as the baselines. In addition, the reclassified cropping intensity results (Section 3.3.3) are used to facilitate the comparison with these products. A positive value indicates that our estimated result has a higher number of cropping cycle(s) than the reference products, while a negative value indicates the opposite. Bearing these in mind, we found that our estimations are generally consistent with those derived from VIP4 and MCD12Q2, although the CI difference shows a range from −3 to 2 (Figs. 10 and 11).

Fig. 10 displays the spatial pattern and statistics of CI difference between our estimations and the 2014 VIP4 output in each region. Our results show overall higher CI estimation than VIP4 in AF, NA, SEA and WE with mean difference values of 0.537, 0.020, 0.218 and 0.174,

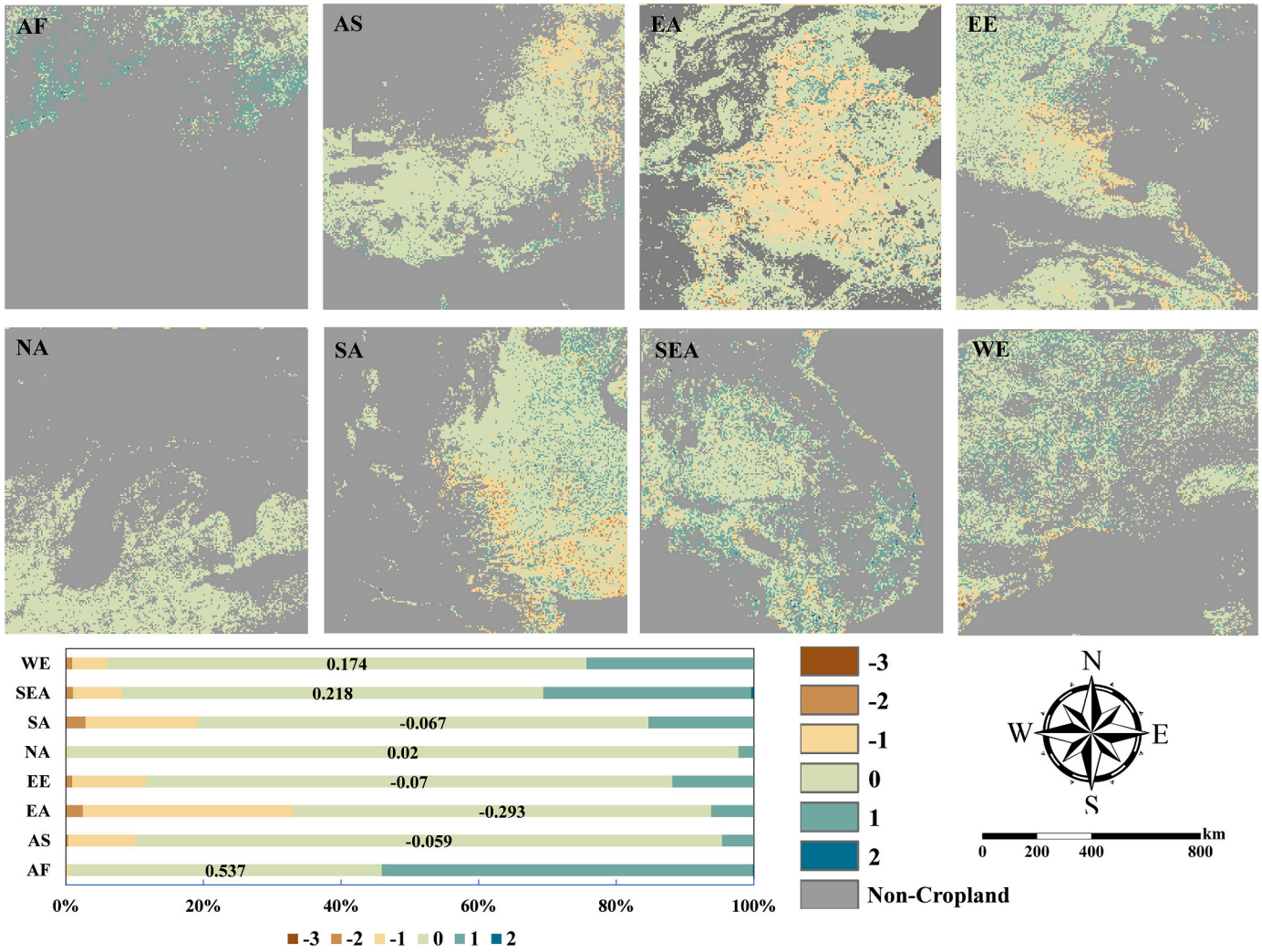

Fig. 10. Spatial patterns and statistics of CI difference between our estimations and the 2014 VIP4 outputs. The number on each bar represents the average difference value.

respectively. In contrast, overall lower estimations by our outputs are observed in the other four regions with mean difference values of −0.059 (AS), −0.293 (EA), −0.07 (EE) and −0.067 (SA). The majority area of pixels with disagreement (i.e., non-zero difference) are associated with only one-cycle difference. The strongest agreement is found in NA (over 96% of zero values), followed by AS and EE with over 75% of agreement. In WE and SEA (about 60–70% of agreement), there are more pixels showing positive values, while in SA and EA the other way is observed. The lowest agreement level occurs in AF, where more than half of the estimations show one more cycle than the VIP4 output. The spatial patterns of the agreement level also vary across regions. Among the three regions with clear patterns of positive values (AF, SEA, WE), inconsistent estimations of cropping cycles in AF are concentrated along the coastline while those in SEA and WE appear scattered. In SA, a number of positive values are sparsely distributed in the north part, and a similar amount of negative values are spotted in south and southwest. For the three regions with observable negative differences (AS, EA, EE), the pattern of CI disagreement in EA is conspicuous as a large patch occupying the central part, while the patches of negative values in AS and EE appear diluted. Finally, in NA where almost no negative difference is found, a few positive values can be vaguely detected.

Compared to the agreement level with VIP4, the statistical differences and corresponding spatial distributions between our CI estimates and MCD12Q2 outputs have a higher level of agreement, although the spatial patterns are fairly heterogeneous (Fig. 11). Based on the statistics, the percentages of pixels with zero difference (i.e., our estimated CI value equals to the value in MCD12Q2) reach 50% or higher for all the study regions. Positive mean difference values are detected in six out of the eight regions, including AF (0.327), EA (0.105), EE (0.086), NA (0.079), SEA (0.175) and WE (0.215). The other two regions, AS and SA, exhibit overall negative values with average differences of −0.005 and −0.021, respectively. Among the eight regions, the largest disagreement stands out in AF where over 30% of the total area have positive values, and considerable positive values are also found in WE, SEA, EA, EE and SA (12%–23%) and fewer in NA (7%) and AS (< 3%). In contrast, SA has an outstanding percentage of negative values (20%), but near zero negative values were found in NA and AF. Other regions hold relatively small percentages of negative values (approximately 2–3%). Spatially, the pattern of positive values is visually detectable in four regions (AF, EA, SEA and WE), while the negative pattern appears only in the SA region, except a few spots along the east part of the AS region (Fig. 11, upper panel). Positive differences of cropping cycle in AF and SEA tend to be located in the coastal region and more sensitive to ocean climates, while in EA and WE, the distributions of positive values are more dispersed and complex. In the rest of the study regions (EE, AS, NA), patterns of disagreement, either positive or negative, are indiscernible, which in turn demonstrates an evident agreement between our estimates and MCD12Q2 outputs.

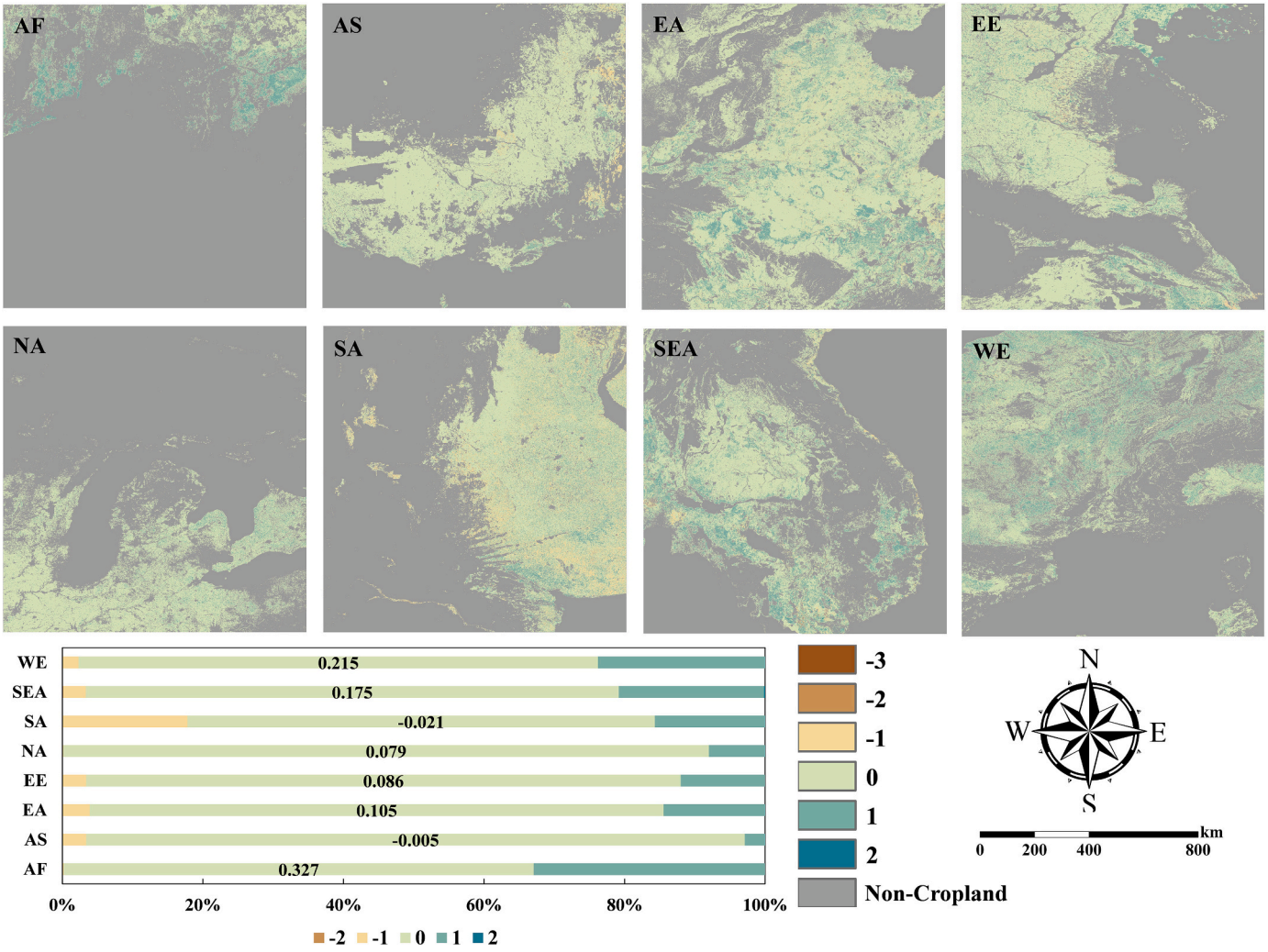

Fig. 11. Spatial patterns and statistics of CI difference between our estimations and the 2016–2017 averaged MCD12Q2 outputs. The number on each bar represents the average difference value.

5. Discussion

5.1. Mapping global cropping intensity at fine resolution

Cropland is among the most complex land use types because it is influenced by both natural processes and anthropogenic drivers as well as their interactions (Li et al., 2014; Belgiu and Csillik, 2018; Liu et al., 2020). The diversity of worldwide cropland in agro-environmental conditions, social-economic levels and management practices makes global cropping intensity mapping a challenging task. Thanks to the open source of the rich data archive of satellite images (Woodcock et al., 2008; Claverie et al., 2018), research relying on remote sensing techniques has made huge progress towards the goal of capturing comprehensive information of cropland, such as cropping extent, crop phenological dynamics, and related human activities for agricultural intensification (Whitcraft et al., 2019). Some existing products, including VIP4 and MCD12Q2, have manifested remarkable achievements of deriving land surface phenology, encompassing information highly relevant to cropping intensity. However, these products are not specifically for cropland, and most of them bear with coarse spatial resolutions, hence raising the within-pixel contamination issue by non-cropland components. This issue is even more crucial in places where croplands are often delimited and managed in small pieces, such as those in Africa and Southeast Asia (Kontgis et al., 2015; Nabil et al., 2020).

In addition to these efforts at the global or continental scale, other researchers have attempted to map CI at the regional or local level from different perspectives. Instead of scrambling to reach a global product with more generalizable algorithms, they seek to approach rather high spatial resolution outputs within a bounded region in complementary or alternative ways. For example, Liu et al. (2020) proposed an algorithm to fuse multi-source satellite images to obtain fine resolution signals of cropping cycles, and then applied their approach for croplands in mainland China. Nevertheless, their implementation relies on empirical rules that are regionally specific (e.g., spectral thresholds for detecting the between-season troughs), so the rule-based recalibration and validation are required before adapting the methods in other regions. In summary, existing research endeavors are facing two inherently limitations, one pertaining to a generalizable CI mapping algorithm at the global scale and the other concerning the fine spatial resolution with the aim of minimizing non-cropland contamination.

In this study, we explicitly address these two inter-connected challenges in CI mapping by designing a new framework that is more self-adaptive and straightforward for global-scale implementation. We tested the proposed framework in eight representative geographic regions with varying biophysical (e.g., climate, topography) and human-influencing (e.g., agricultural systems, cropland parcel size) conditions, and obtained overall satisfactory results. The main advantages of the new framework are threefold.

First, compared to existing global products derived from coarse

resolution instruments like AVHRR (1000-m) or MODIS (from 250-m to 1000-m), our CI estimation offers a much higher spatial resolution (30-m). Higher spatial resolution CI information is not only statistically useful for more accurate estimations regarding cropland management but also highly beneficial to the detection of subtle patterns within heterogeneous landscape, both of which are essential to better understand cropland use dynamics with anthropogenic activities (Belgiu and Csillik, 2018). These benefits are illustrated by a schematic comparison among high resolution Google Earth image (true color as a reference), our estimates (30-m), MCD12Q1 (500-m), and VIP4 (0.05°) based on a zoomed-in scene in northeast Argentina (Fig. S3). With an improved resolution, our estimation is associated with reduced uncertainty caused by sub-pixel heterogeneity, and is capable of revealing the hidden patterns of double cropping that would otherwise not be detected using coarse resolution products. Apart from the improvement of mapping accuracy, the 30-m CI data will potentially facilitate fine-scale agricultural research that was previously not applicable. For example, the new framework is particularly valuable for monitoring farming practices by smallholders, which constitutes over 50% of rural populations in developing countries that are most vulnerable to food security and environmental challenges (Morton et al., 2006; Jain et al., 2013). The finer-level monitoring of cropping activities would also make it possible for agricultural conservation initiatives targeting and prioritizing the least resilient farm groups.

Second, the new framework provides the possibility of more generalizable CI mapping compared to previous studies at the regional or local scale (e.g., Li et al., 2012; Kontgis et al., 2015; Liu et al., 2020). Rather than directly adopting the NDVI trajectory, the CI information in this study is derived from the binary phenophase time series (Fig. 3), so the impacts of background noises incurred by unfavorable weather conditions and non-agricultural land covers can be greatly reduced or even eliminated. As a result, the framework can be applied to various agro-ecological zones without much users' intervention. Moreover, the binary phenophase time series is less sensitive to data inconsistence, having the feasibility of integrating more data types (e.g., Synthetic Aperture Radar) for CI mapping.

Finally, the utilization of the GEE platform enables efficient and effective CI mapping over a large spatial extent. With the ability of high computing performance, GEE has been employed for the production of global datasets, including forest (Hansen et al., 2013), surface water (Pekel et al., 2016; Pickens et al., 2020) and artificial impervious area (Gong et al., 2020). Similar to the experiences of these successful studies, we found that GEE speeds up the entire process of the proposed CI mapping to a considerable degree (less than 12 h for each 10° × 10° region), which lays a solid foundation for its application at the planetary scale.

5.2. Factors affecting the accuracy of cropping intensity mapping

Although the framework presents substantial confidence regarding the global mapping of fine resolution CI, our analysis also indicates several issues that bear attention. The availability of reliable cropland extent data, which can be derived from either land cover products such as GlobeLand30 (Chen et al., 2015) and FROM-GLC (Gong et al., 2013) or specific cropland/non-cropland maps, has always been a critical constraint on cropland-based applications, such as CI mapping (Gray et al., 2014a). For this work, we selected GFSAD30 as the base cropland/non-cropland map, which provides the 30-m distribution of global cropland that is explicitly distinguished from other land cover types. Despite overall high accuracies, classification errors still exist in GFSAD30 (Xiong et al., 2017), even after a refinement procedure to combine it with three additional land cover products. In particular, we found less desirable performances of the cropland/non-cropland layer in AF and SA (Fig. 5), which is likely due to the inclusion of some grasslands as cropland extents in GFSAD 30 (Fig. S4). These errors are likely to be propagated to the final CI outputs, making the validation and comparison results (especially those statistics) less informative.

During the process of constructing time series, we smoothed NDVI time-series data by incorporating multiple satellite sensors, including Landsat, Sentinel-2 and MODIS, aiming to increase the frequency of clear-sky observations. The reconstructed NDVI image cubes, with a temporal resolution of 16-day, prove to work well in general for modeling the phenological behavior of cropping intensity. Nevertheless, a few outliers, particularly in cloudy, tropical regions where missing observations are common, persist according to our evaluation (Fig. 6). Additionally, the regression-based data gap filling from MODIS can be influenced by the mismatch of spatial resolutions (i.e., 30-m versus 250-m) and spectral bandwidths, both of which can result in the less satisfactory regression performance, especially in more heterogeneous areas (Fig. S5).

The identification of phenophase cycles is also associated with assumptions that should be further verified. In this study, we adopt the threshold of 50% of the NDVI amplitude as the transition point to identify crop phenophase cycles. This threshold assumption, however, may be violated in extreme but rare cases. For example, in Northeast China, it is common practice to plant more than one crop types in the same field. Such a cropping strategy would result in a nuanced shallow trough in NDVI time series due to the different harvest time (Gray et al., 2014a), which would probably cause our framework less reliable in these particular areas.

Comprehensive assessment of CI mapping accuracy continues facing challenges primarily due to the lack of directly comparable reference (Li et al., 2014; Kontgis et al., 2015). In this study, we use three assessment data sources: the PhenoCam network, collected samples and comparable land surface phenology products. Given the capacity of depicting phenological signals across the whole canopy, the PhenoCam network provides the most valuable information for CI accuracy assessment. Unfortunately, the network of PhenoCam spots is sparse on cropland with relatively short temporal coverage, limiting its worldwide applications. Moreover, the scale mismatch between near-ground measurement footprint and satellite image pixel size (i.e., 30-m) can bring additional uncertainties for CI estimation (Fig. S2). Regarding the second validation source, the collected samples are extracted through visual interpretation of multiple NDVI time-series data, which inevitably contains errors (Foody et al., 2016). Besides, there may exist an imbalanced sampling among different cropping types, that is, the sample size is limited for cropland with higher CI values. In particular, some continuous cropping pixels were identified based on the CV values of the collected samples (i.e., RD-2), and a small size of sample may lead to less reliable classification of the continuous cropping type. This is evident by its wide range of accuracy assessment (50%–100%) as shown in Table 2. In terms of the last data source for testing the agreement level, we use two land surface phenology products (VIP4 and MCD12Q2) to conduct pixel by pixel comparisons. In addition to the spatial mismatch mentioned above, another primary cause of the CI difference may be the inconsistent algorithm structures of identifying phenological seasons. In particular, in our estimates and MCD12Q2, a valid phenology season should include both greenup and greendown segments, whereas in VIP4 this requirement is not needed, possibly resulting in the “partial seasons”. Such discrepancy is likely to explain most of the CI difference due to the planting of winter wheat in the North China Plain (the EA tile in Fig. 10).

5.3. Methodological and practical implications

This study offers both methodological and practical implications from the implementation of our CI mapping framework, directing to a plethora of potential future endeavors. Methodologically, there is room for improvement in each of the main components of the current framework. The derivation of cropping intensity specific to crop phenology requires as sufficiently accurate cropland extent as possible to be commensurate with the spatial scale of interest (i.e., 30-m). In this

study, the extraction of cropland area mainly relies on the accuracy of GFSAD30, and other three complementary products (FNF, GSWL, and GHSL). To achieve a more reliable cropland extent, many other products or methods can be taken advantage of, while the way of multi-source integration should be carefully paved. For example, grassland pixels displaying low seasonality can be effectively removed from the cropland layer in GFSAD30 by setting a lower NDVI amplitude threshold, although such a thresholding procedure may cause omission errors in areas with low density of planting crops.

As another critical step in generating continuous NDVI signals, time series smoothing can impact the determination of thresholds that identify crop phenophase(s). The refinement of data smoothing can focus not only on incorporating more reliable observations from improved satellite archives, such as the Harmonized Landsat and Sentinel-2 (HLS) surface reflectance dataset (Claverie et al., 2018), but also on a more suitable smoothing parameter(s) that seeks to balance handling outliers and retaining seasonality. In the determination of transition points of crop phenology, systematic testing and identification of the phenophase are of paramount importance for outcome sensitivity. In this study, we adopt the most widely applied greenness index, NDVI, for the representation of crop phenological trends, which might be different from those derived from an alternative index (e.g., Enhanced Vegetation Index). Meanwhile, more auxiliary data, in addition to vegetation indices, can also be useful to enhance the robustness of period segmentation. For instance, land surface temperature (LST) information can be leveraged to limit the potential growing periods (Dong et al., 2016), while Land Surface Water Index (LSWI) may be better at informing multiple-season rice planting (Ding et al. 2020). Last but not least, within the current scope, we only select eight geographic regions with an emphasis on testing algorithm performance, which limits the use of existing field measurements outside the study regions. When moving onto the product generation of global CI maps, a more comprehensive validation using all available in-situ observations (e.g., the FLUXNET network) can consolidate the reliability of the current algorithms.

As a milestone that dovetails this study, the Version 1 global CI product at the 30-m resolution is currently under development for the period of 2016–2018, and will be publicly available in the near future. We expect that the product will provide the user community with new insights into the global agriculture practices that have not been fully reflected in existing datasets, and therefore enlighten innovative cropland management by public and non-governmental sectors. Moreover, given the worldwide CI distribution with fine spatial resolution, relevant studies with more sophisticated and comprehensive ideas will be possibly crafted. For example, multiple cropping, as one type of agricultural intensification, can help explain some of the seasonal variations in global carbon uptake (Gray et al., 2014b), thus carrying the potential for combating climate change under current and future scenarios. Finally, using this product as the baseline, along with the integration of time-series algorithms, the study may be extended to monitor the spatial-temporal dynamics of global CI over the past decades, making it possible to examine their drivers from both biotic and abiotic processes. Only by fully understanding such complex processes can the sustainable development goals be better achieved.

6. Conclusions

Fine resolution mapping of global CI is a challenging task from almost every aspect of remote sensing, including data acquisition, cropland extent extraction, time series modeling, phenological cycle identification and accuracy assessment. In this study, we develop a novel framework for CI estimation using multiple satellite data and the GEE platform. Experimental results in eight representative regions across the globe reveal the feasibility of this framework. Three major conclusions can be reached. First, the integration of multi-source satellite data, including Landsat, Sentinel-2 and resampled MODIS, shows a great potential of revealing cropping practices with high spatial (30-m) and temporal (16-day) resolutions, which can facilitate the detection of multiple cropping systems with applications of cropland management by smallholders. Second, the utilization of binary phenophase profile rather than original vegetation greenness time series reduce additional uncertainties, and is demonstrated to be highly self-adaptive for CI identification across continents with varying biophysical and anthropogenic contextual settings. Finally, the global CI estimation should embrace advanced computing platforms such as GEE to improve mapping efficiency and effectiveness. We expect that the continuing endeavor of generating global CI products under our framework will benefit a variety of scientific researches on agriculture in line with the zero-hunger goal by the United Nations.

Declaration of Competing Interest

The authors declare that they have no known competing financial interests or personal relationships that could have appeared to influence the work reported in this paper.

Acknowledgements

This research was supported by National Key R&D Program of China (2016YFA0600302, 2016YFD0300608), National Natural Science Foundation of China (41561144013, 41761144064, 41701496, 41761020) and the Key Collaborative Research Program of the Alliance of International Science Organizations (ANSO-CR-KP-2020-07). The development of PhenoCam has been funded by the Northeastern States Research Cooperative, NSF's Macrosystems Biology program (awards EF-1065029 and EF-1702697), and DOE's Regional and Global Climate Modeling program (award DE-SC0016011). We acknowledge additional support from the US National Park Service Inventory and Monitoring Program and the USA National Phenology Network (grant number G10AP00129 from the United States Geological Survey), and from the USA National Phenology Network and North Central Climate Science Center (cooperative agreement number G16AC00224 from the United States Geological Survey). Additional funding, through the National Science Foundation's LTER program, has supported research at Harvard Forest (DEB-1237491) and Bartlett Experimental Forest (DEB-1114804). We also thank the USDA Forest Service Air Resource Management program and the National Park Service Air Resources program for contributing their camera imagery to the PhenoCam archive. The authors would like to thank the editor and anonymous reviewers for their constructive and insightful comments on an earlier draft of this paper.

Appendix A. Supplementary data

Supplementary data to this article can be found online at https://doi.org/10.1016/j.rse.2020.112095.

References

Alexandratos, N., Bruinsma, J., 2012. World Agriculture towards 2030/2050: The 2012 Revision.

Bayas, J.C.L., Lesiv, M., Waldner, F., Schucknecht, A., Duerauer, M., See, L., Fritz, S., Fraisl, D., Moorthy, I., McCallum, I., Perger, C., 2017. A global reference database of crowdsourced cropland data collected using the geo-wiki platform. Sci. Data 4, 170136.

Belgiu, M., Csillik, O., 2018. Sentinel-2 cropland mapping using pixel-based and object-based time-weighted dynamic time warping analysis. Remote Sens. Environ. 204, 509–523.

Bolton, D.K., Gray, J.M., Melaas, E.K., Moon, M., Eklundh, L., Friedl, M.A., 2020. Continental-scale land surface phenology from harmonized Landsat 8 and Sentinel-2 imagery. Remote Sens. Environ. 240, 111685.

Chastain, R., Housman, I., Goldstein, J., Finco, M., Tenneson, K., 2019. Empirical cross sensor comparison of sentinel-2A and 2B MSI, Landsat-8 OLI, and Landsat-7 ETM+ top of atmosphere spectral characteristics over the conterminous United States. Remote Sens. Environ. 221, 274–285.

Chen, B., 2018. Globally increased crop growth and cropping intensity from the long-term satellite-based observations. ISPRS Ann. Photogram. Remote Sens. Spatial Inform. Sci. 4 (3).
Chen, J., Chen, J., Liao, A., Cao, X., Chen, L., Chen, X., He, C., Han, G., Peng, S., Lu, M., Zhang, W., 2015. Global land cover mapping at 30 m resolution: a POK-based operational approach. ISPRS J. Photogramm. Remote Sens. 103, 7–27.
Claverie, M., Ju, J., Masek, J.G., Dungan, J.L., Vermote, E.F., Roger, J.C., Skakun, S.V., Justice, C., 2018. The harmonized Landsat and Sentinel-2 surface reflectance data set. Remote Sens. Environ. 219, 145–161.
d'Amour, C.B., Reitsma, F., Baiocchi, G., Barthel, S., Güneralp, B., Erb, K.H., Haberl, H., Creutzig, F., Seto, K.C., 2017. Future urban land expansion and implications for global croplands. Proc. Natl. Acad. Sci. 114 (34), 8939–8944.
Didan, K., Barreto, A., 2016. NASA MEaSUREs vegetation index and phenology (VIP) vegetation indices monthly global 0.05 Deg CMG. In: NASA EOSDIS Land Process. DAAC, pp. 4.
Ding, M., Chen, Q., Xiao, X., Xin, L., Zhang, G., Li, L., 2016. Variation in cropping intensity in northern China from 1982 to 2012 based on GIMMS-NDVI data. Sustainability 8 (11) p.1123.
Ding, M., Guan, Q., Li, L., Zhang, H., Liu, C., Zhang, L., 2020. Phenology-based rice paddy mapping using multi-source satellite imagery and a fusion algorithm applied to the poyang lake plain, southern china. Remote Sens. 12 (6), 1022.
Dong, J., Xiao, X., Menarguez, M.A., Zhang, G., Qin, Y., Thau, D., Biradar, C., Moore III, B., 2016. Mapping paddy rice planting area in northeastern Asia with Landsat 8 images, phenology-based algorithm and Google earth engine. Remote Sens. Environ. 185, 142–154.
Eilers, P.H., 2003. A perfect smoother. Anal. Chem. 75 (14), 3631–3636.
Eilers, P.H., Pesendorfer, V., Bonifacio, R., 2017, June. Automatic smoothing of remote sensing data. In: 2017 9th International Workshop on the Analysis of Multitemporal Remote Sensing Images (MultiTemp). IEEE, pp. 1–3.
Foley, J.A., Ramankutty, N., Brauman, K.A., Cassidy, E.S., Gerber, J.S., Johnston, M., Mueller, N.D., O'Connell, C., Ray, D.K., West, P.C., Balzer, C., 2011. Solutions for a cultivated planet. Nature 478 (7369), 337–342.
Foody, G.M., Pal, M., Rocchini, D., Garzon-Lopez, C.X., Bastin, L., 2016. The sensitivity of mapping methods to reference data quality: Training supervised image classifications with imperfect reference data. ISPRS Int. J. Geo Inf. 5 (11), 199.
Frasso, G., Eilers, P.H., 2015. L-and V-curves for optimal smoothing. Stat. Model. 15 (1), 91–111.
Godfray, H.C.J., Beddington, J.R., Crute, I.R., Haddad, L., Lawrence, D., Muir, J.F., Pretty, J., Robinson, S., Thomas, S.M., Toulmin, C., 2010. Food security: the challenge of feeding 9 billion people. Science 327 (5967), 812–818.
Gong, P., Wang, J., Yu, L., Zhao, Y., Zhao, Y., Liang, L., Niu, Z., Huang, X., Fu, H., Liu, S., Li, C., 2013. Finer resolution observation and monitoring of global land cover: first mapping results with Landsat TM and ETM+ data. Int. J. Remote Sens. 34 (7), 2607–2654.
Gong, P., Li, X., Wang, J., Bai, Y., Chen, B., Hu, T., Liu, X., Xu, B., Yang, J., Zhang, W., Zhou, Y., 2020. Annual maps of global artificial impervious area (GAIA) between 1985 and 2018. Remote Sens. Environ. 236, 111510.
Gorelick, N., Hancher, M., Dixon, M., Ilyushchenko, S., Thau, D., Moore, R., 2017. Google earth engine: planetary-scale geospatial analysis for everyone. Remote Sens. Environ. 202, 18–27.
Gray, J., Friedl, M., Frolking, S., Ramankutty, N., Nelson, A., Gumma, M.K., 2014a. Mapping Asian cropping intensity with MODIS. IEEE J. Selected Topics Appl. Earth Observ. Remote Sens. 7 (8), 3373–3379.
Gray, J., Frolking, S., Kort, E.A., Ray, D.K., Kucharik, C.J., Ramankutty, N., Friedl, M.A., 2014b. Direct human influence on atmospheric CO_2 seasonality from increased cropland productivity. Nature 515 (7527), 398–401.
Gray, J.M., Sulla-menashe, D., Friedl, M.A., 2019. User Guide to Collection 6 MODIS Land Cover Dynamics (MCD12Q2) Product. [WWW Document]. URL. https://lpdaac.usgs.gov/documents/218/mcd12q2_v6_user_guide.pdf.
Gross, A.M., 1977. Confidence intervals for bisquare regression estimates. J. Am. Stat. Assoc. 72 (358), 341–354.
Gumma, M.K., Thenkabail, P.S., Teluguntla, P.G., Oliphant, A., Xiong, J., Giri, C., Pyla, V., Dixit, S., Whitbread, A.M., 2020. Agricultural cropland extent and areas of South Asia derived using Landsat satellite 30-m time-series big-data using random forest machine learning algorithms on the Google earth engine cloud. GISci. Remote Sens. 57 (3), 302–322.
Hansen, M.C., Potapov, P.V., Moore, R., Hancher, M., Turubanova, S.A., Tyukavina, A., Thau, D., Stehman, S.V., Goetz, S.J., Loveland, T.R., Kommareddy, A., 2013. High-resolution global maps of 21st-century forest cover change. science 342 (6160), 850–853.
Iizumi, T., Ramankutty, N., 2015. How do weather and climate influence cropping area and intensity? Global Food Security 4, 46–50.
Jain, M., Mondal, P., DeFries, R.S., Small, C., Galford, G.L., 2013. Mapping cropping intensity of smallholder farms: a comparison of methods using multiple sensors. Remote Sens. Environ. 134, 210–223.
Kastner, T., Rivas, M.J.I., Koch, W., Nonhebel, S., 2012. Global changes in diets and the consequences for land requirements for food. Proc. Natl. Acad. Sci. 109 (18), 6868–6872.
Kong, D., Zhang, Y., Gu, X., Wang, D., 2019. A robust method for reconstructing global MODIS EVI time series on the Google earth engine. ISPRS J. Photogramm. Remote Sens. 155, 13–24.
Kontgis, C., Schneider, A., Ozdogan, M., 2015. Mapping rice paddy extent and intensification in the Vietnamese Mekong River Delta with dense time stacks of Landsat data. Remote Sens. Environ. 169, 255–269.
Lavreniuk, M., Shelestov, A., Kolotii, A., Vasiliev, V., Shumilo, L., Kussul, N., 2018. Automated System for Crop Mapping in Amazon web Services Based on Sentinel Data. EGUGA, pp. 16629.
Li, P., Feng, Z., Jiang, L., Liu, Y., Xiao, X., 2012. Changes in rice cropping systems in the Poyang Lake region, China during 2004–2010. J. Geogr. Sci. 22 (4), 653–668.
Li, L., Friedl, M.A., Xin, Q., Gray, J., Pan, Y., Frolking, S., 2014. Mapping crop cycles in China using MODIS-EVI time series. Remote Sens. 6 (3), 2473–2493.
Liu, C., Xiong, T., Gong, P., Qi, S., 2018. Improving large-scale moso bamboo mapping based on dense Landsat time series and auxiliary data: a case study in Fujian Province, China. Remote Sens. Lett. 9 (1), 1–10.
Liu, C., Zhang, Q., Luo, H., Qi, S., Tao, S., Xu, H., Yao, Y., 2019. An efficient approach to capture continuous impervious surface dynamics using spatial-temporal rules and dense Landsat time series stacks. Remote Sens. Environ. 229, 114–132.
Liu, L., Xiao, X., Qin, Y., Wang, J., Xu, X., Hu, Y., Qiao, Z., 2020. Mapping cropping intensity in China using time series Landsat and Sentinel-2 images and Google earth engine. Remote Sens. Environ. 239, 111624.
Moon, M., Zhang, X., Henebry, G.M., Liu, L., Gray, J.M., Melaas, E.K., Friedl, M.A., 2019. Long-term continuity in land surface phenology measurements: a comparative assessment of the MODIS land cover dynamics and VIIRS land surface phenology products. Remote Sens. Environ. 226, 74–92.
Morton, D.C., DeFries, R.S., Shimabukuro, Y.E., Anderson, L.O., Arai, E., del Bon Espirito-Santo, F., Freitas, R., Morisette, J., 2006. Cropland expansion changes deforestation dynamics in the southern Brazilian Amazon. Proc. Natl. Acad. Sci. 103 (39), 14637–14641.
Nabil, M., Zhang, M., Bofana, J., Wu, B., Stein, A., Dong, T., Zeng, H., Shang, J., 2020. Assessing factors impacting the spatial discrepancy of remote sensing based cropland products: a case study in Africa. Int. J. Appl. Earth Obs. Geoinf. 85, 102010.
Oliphant, A.J., Thenkabail, P.S., Teluguntla, P., Xiong, J., Gumma, M.K., Congalton, R.G., Yadav, K., 2019. Mapping cropland extent of southeast and Northeast Asia using multi-year time-series Landsat 30-m data using a random forest classifier on the Google earth engine cloud. Int. J. Appl. Earth Obs. Geoinf. 81, 110–124.
Pekel, J.F., Cottam, A., Gorelick, N., Belward, A.S., 2016. High-resolution mapping of global surface water and its long-term changes. Nature 540 (7633), 418–422.
Phalke, A.R., Özdoğan, M., Thenkabail, P.S., Erickson, T., Gorelick, N., Yadav, K., Congalton, R.G., 2020. Mapping croplands of Europe, Middle East, Russia, and Central Asia using Landsat, random Forest, and Google earth engine. ISPRS J. Photogramm. Remote Sens. 167, 104–122.
Pickens, A.H., Hansen, M.C., Hancher, M., Stehman, S.V., Tyukavina, A., Potapov, P., Marroquin, B., Sherani, Z., 2020. Mapping and sampling to characterize global inland water dynamics from 1999 to 2018 with full Landsat time-series. Remote Sens. Environ. 243, 111792.
Pingali, P.L., 2012. Green revolution: impacts, limits, and the path ahead. Proc. Natl. Acad. Sci. 109 (31), 12302–12308.
Qi, J., Katic, P., Mukherji, A., Ruhweza, A., Spierenburg, M., 2020. Rethinking Global Security. In, Our Future on Earth, pp. 75.
Qiu, S., Zhu, Z., He, B., 2019. Fmask 4.0: improved cloud and cloud shadow detection in Landsats 4–8 and Sentinel-2 imagery. Remote Sens. Environ. 231, 111205.
Qiu, T., Song, C., Zhang, Y., Liu, H., Vose, J.M., 2020. Urbanization and climate change jointly shift land surface phenology in the northern mid-latitude large cities. Remote Sens. Environ. 236, 111477.
Richardson, A.D., Hufkens, K., Milliman, T., Aubrecht, D.M., Chen, M., Gray, J.M., Johnston, M.R., Keenan, T.F., Klosterman, S.T., Kosmala, M., Melaas, E.K., 2018. Tracking vegetation phenology across diverse north American biomes using PhenoCam imagery. Sci. Data 5, 180028.
Sakti, A.D., Takeuchi, W., 2018. Estimation of global crop calendar and intensity using the MODIS NDVI Time Series from 2001 to 2015. In: International Symposium on Remote Sensing.
Scheffler, D., Frantz, D., Segl, K., 2020. Spectral harmonization and red edge prediction of Landsat-8 to Sentinel-2 using land cover optimized multivariate regressors. Remote Sens. Environ. 241, 111723.
Seyednasrollah, B., Young, A.M., Hufkens, K., Milliman, T., Friedl, M.A., Frolking, S., Richardson, A.D., 2019. Tracking vegetation phenology across diverse biomes using version 2.0 of the PhenoCam dataset. Sci. Data 6 (1), 1–11.
Siebert, S., Portmann, F.T., Döll, P., 2010. Global patterns of cropland use intensity. Remote Sens. 2 (7), 1625–1643.
Singha, M., Dong, J., Zhang, G., Xiao, X., 2019. High resolution paddy rice maps in cloud-prone Bangladesh and Northeast India using Sentinel-1 data. Sci. Data 6 (1), 1–10.
Taylor, K.E., 2001. Summarizing multiple aspects of model performance in a single diagram. J. Geophys. Res.-Atmos. 106 (D7), 7183–7192.
Teluguntla, P., Thenkabail, P.S., Oliphant, A., Xiong, J., Gumma, M.K., Congalton, R.G., Yadav, K., Huete, A., 2018. A 30-m landsat-derived cropland extent product of Australia and China using random forest machine learning algorithm on Google earth engine cloud computing platform. ISPRS J. Photogramm. Remote Sens. 144, 325–340.
Tilman, D., Balzer, C., Hill, J., Befort, B.L., 2011. Global food demand and the sustainable intensification of agriculture. Proc. Natl. Acad. Sci. 108 (50), 20260–20264.
UN, 2015. Resolution Adopted by the General Assembly on 25 September 2015.
Van Dijk, A.I., Beck, H.E., Crosbie, R.S., de Jeu, R.A., Liu, Y.Y., Podger, G.M., Timbal, B., Viney, N.R., 2013. The millennium drought in Southeast Australia (2001–2009): natural and human causes and implications for water resources, ecosystems, economy, and society. Water Resour. Res. 49 (2), 1040–1057.
Whitcraft, A.K., Becker-Reshef, I., Justice, C.O., Gifford, L., Kavvada, A., Jarvis, I., 2019. No pixel left behind: toward integrating earth observations for agriculture into the United Nations sustainable development goals framework. Remote Sens. Environ. 235, 111470.
Whittaker, E.T., 1922. On a new method of graduation. In: Proceedings of the Edinburgh Mathematical Society. 41. pp. 63–75.
Wilder, B., 2012. Cloud Architecture Patterns: Using Microsoft Azure. O'Reilly Media, Inc.

Woodcock, C.E., Allen, R., Anderson, M., Belward, A., Bindschadler, R., Cohen, W., Gao, F., Goward, S.N., Helder, D., Helmer, E., Nemani, R., 2008. Free access to Landsat imagery. Science 320 (5879), 1011.
Wu, B., Zhang, M., Zeng, H., Liu, G., Chang, S., Gommes, R., 2014. New indicators for global crop monitoring in CropWatch-case study in North China Plain. In: IOP Conference Series: Earth and Environmental Science. Vol. 17. IOP Publishing, pp. 012050 No. 1.
Wu, B., Gommes, R., Zhang, M., Zeng, H., Yan, N., Zou, W., Zheng, Y., Zhang, N., Chang, S., Xing, Q., Van Heijden, A., 2015. Global crop monitoring: a satellite-based hierarchical approach. Remote Sens. 7 (4), 3907–3933.
Wu, W., Yu, Q., You, L., Chen, K., Tang, H., Liu, J., 2018. Global cropping intensity gaps: increasing food production without cropland expansion. Land Use Policy 76, 515–525.
Xie, H., Huang, Y., Chen, Q., Zhang, Y., Wu, Q., 2019. Prospects for agricultural sustainable intensification: a review of research. Land 8 (11), 157.
Xiong, J., Thenkabail, P.S., Tilton, J.C., Gumma, M.K., Teluguntla, P., Oliphant, A., Congalton, R.G., Yadav, K., Gorelick, N., 2017. Nominal 30-m cropland extent map of continental Africa by integrating pixel-based and object-based algorithms using Sentinel-2 and Landsat-8 data on Google earth engine. Remote Sens. 9 (10), 1065.
Xu, H., Qi, S., Gong, P., Liu, C., Wang, J., 2018. Long-term monitoring of citrus orchard dynamics using time-series Landsat data: a case study in southern China. Int. J. Remote Sens. 39 (22), 8271–8292.
Yan, H., Xiao, X., Huang, H., Liu, J., Chen, J., Bai, X., 2014. Multiple cropping intensity in China derived from agro-meteorological observations and MODIS data. Chin. Geogr. Sci. 24 (2), 205–219.
Yan, H., Liu, F., Qin, Y., Doughty, R., Xiao, X., 2019. Tracking the spatio-temporal change of cropping intensity in China during 2000–2015. Environ. Res. Lett. 14 (3), 035008.
Zaks, D.P., Kucharik, C.J., 2011. Data and monitoring needs for a more ecological agriculture. Environ. Res. Lett. 6 (1), 014017.
Zalles, V., Hansen, M.C., Potapov, P.V., Stehman, S.V., Tyukavina, A., Pickens, A., Song, X.P., Adusei, B., Okpa, C., Aguilar, R., John, N., 2019. Near doubling of Brazil's intensive row crop area since 2000. Proc. Natl. Acad. Sci. 116 (2), 428–435.
Zhang, X., 2015. Reconstruction of a complete global time series of daily vegetation index trajectory from long-term AVHRR data. Remote Sens. Environ. 156, 457–472.
Zhang, Y., Song, C., Sun, G., Band, L.E., McNulty, S., Noormets, A., Zhang, Q., Zhang, Z., 2016. Development of a coupled carbon and water model for estimating global gross primary productivity and evapotranspiration based on eddy flux and remote sensing data. Agric. For. Meteorol. 223, 116–131.
Zhang, X., Jayavelu, S., Liu, L., Friedl, M.A., Henebry, G.M., Liu, Y., Schaaf, C.B., Richardson, A.D., Gray, J., 2018. Evaluation of land surface phenology from VIIRS data using time series of PhenoCam imagery. Agric. For. Meteorol. 256, 137–149.
Zhu, Z., Woodcock, C.E., 2012. Object-based cloud and cloud shadow detection in Landsat imagery. Remote Sens. Environ. 118, 83–94.
Zhu, Z., Gallant, A.L., Woodcock, C.E., Pengra, B., Olofsson, P., Loveland, T.R., Jin, S., Dahal, D., Yang, L., Auch, R.F., 2016. Optimizing selection of training and auxiliary data for operational land cover classification for the LCMAP initiative. ISPRS J. Photogramm. Remote Sens. 122, 206–221.